Theses and Dissertations

2015

Band to Band Calibration and Relative Gain Analysis of Satellite Sensors Using Deep Convective Clouds

Suman Bhatta
South Dakota State University

Follow this and additional works at: http://openprairie.sdstate.edu/etd

 Part of the Electrical and Computer Engineering Commons

BAND TO BAND CALIBRATION AND RELATIVE GAIN ANALYSIS OF

SATELLITE SENSORS USING DEEP CONVECTIVE CLOUDS

BY

SUMAN BHATTA

A thesis submitted in partial fulfillment of the requirements for the

Master of Science

Major in Electrical Engineering

South Dakota State University

2015

BAND TO BAND CALIBRATION AND RELATIVE GAIN ANALYSIS OF

SATELLITE SENSORS USING DEEP CONVECTIVE CLOUDS

This thesis is approved as a creditable and independent investigation by a

candidate for the Master of Science in Electrical Engineering degree and is acceptable for

meeting the thesis requirements for this degree. Acceptance of this does not imply that

the conclusions reached by the candidates are necessarily the conclusions of the major

department.

Dr. Dennis Helder
Distinguished Professor and Dean of Research
College of engineering
South Dakota State University
Thesis Advisor   Date

Dr. Steven Hietpas ⁻
Head, Department of Electrical Engineering and
Computer Science   Date

Dr. Kinchel C. Doerner
Dean, Graduate School   Date

ACKNOWLEDGEMENTS

TABLE OF CONTENTS

LIST OF FIGURES

LIST OF TABLES

ABSTRACT

BAND TO BAND CALIBRATION AND RELATIVE GAIN ANALYSIS OF

SATELLITE SENSORS USING DEEP CONVECTIVE CLOUDS

SUMAN BHATTA

2015

Two calibration techniques were developed in this research. First, a calibration

technique, in which calibration was transferred to cirrus band and coastal aerosol band

from well calibrated reflective bands of Landsat 8 using SCIAMACHY Deep Convective

Cloud (DCC) spectra. Second, a novel method to derive relative gains using DCCs and

improve the image quality of cirrus band scenes was developed. DCCs are very cold,

bright clouds located in the tropopause layer. At small sun elevation and sensor viewing

angles, they act as near Lambertian solar reflectors. They have very high signal to noise

ratio and can easily be detected using simple IR threshold. Thus, DCCs are an ideal

calibration target. Cirrus band in Landsat 8 has band center at 1375nm. Due to high water

vapor absorption at this wavelength it is difficult to calibrate the cirrus band using other

standard vicarious calibration methods. Similarly, the coastal aerosol band has short

wavelength (443nm). At this wavelength maximum scattering can be observed in the

atmosphere, due to which it is difficult to calibrate this band. Thus DCCs are investigated

to calibrate these two channels. DCC spectra measured by the SCIAMACHY

hyperspectral sensor were used to transfer calibration. The gain estimates after band to

band calibration using DCC for the coastal aerosol band was 0.986 ±0.0031 and that for

cirrus band was 0.982±0.0398. The primarily target was to estimate gains with

uncertainty of less than 5%. The results are within required precision levels and the primarily goal of the research was successfully accomplished.

The non-uniformity in detector response can cause visible streaks in the image. To remove these visible streaks, modified histogram equalization method was used in the second algorithm. A large number of DCC scenes were binned and relative gains were derived. Results were validated qualitatively by visual analysis and quantitatively by the streaking metric. The streaking metric was below 0.2 for most of the detector which was the required goal. Visible streaks were removed by applying DCC derived gains and in most of the cases DCC gains outperforms the default gains.

CHAPTER 1

1   INTRODUCTION

1.1   Remote Sensing

Remote sensing is the field of study associated with extracting information about an object without coming into physical contact with it [1]. Generally remote sensing refers to the science that investigates and acquires the information of distant object's using various bands of electromagnetic waves ranging from low frequency radio waves to high frequency microwaves up to gamma rays. One of the major purposes of remote sensing is to observe and study the earth's surface, its land, water and atmosphere. Remote sensing gives us a unique opportunity to see the world from a different perspective. Remotely observing the earth surface through various spectra of electromagnetic waves helps us to observe different parameters such as surface temperature, atmospheric water content, land structure, vegetation area and many other properties, which cannot be seen through the naked eyes.

The distant object and its properties can be observed on the basis of radiation directly emitted by the objects being viewed (e.g. thermal self-emission or reflected radiation from natural sources), this type of remote sensing is known as Passive Remote Sensing. In active remote sensing, the sensor itself irradiates the object and then the reradiated energy from the object is observed by the sensor instrument [1].

There are various applications of remote sensing in earth observation. Depending on the user's need, different remote sensing systems have been developed that cover a wide range of spatial, spectral and temporal parameters. Different applications of remote sensing are weather forecasting, determination of temperature, thermal mapping,

engineering geology, geothermal and volcano studies, detecting underground and surface coal fire, land use, land cover mapping, oceanography and marine resources, application of fluorosensing, forest fire, volcanic eruption and flooding [2].

A satellite sensor provides us valuable information about the earth by observing it in various electromagnetic spectrums. But for the successful extraction of data from the earth's surface, the sensor has to see through many hindrances, such as the intervening atmosphere, aerosol's in the atmosphere, clouds, and the ozone layer. Researchers have come out with many solutions to get valuable data without it being spoiled by these hindrances. One such hindrance is cloud that affects the collected information by the sensor. Clouds are of different types. Some are visible in satellite imagery, whereas some types of clouds such as cirrus clouds are not easily visible in satellite imagery [3]. If imagery can be freed from such high altitude cirrus clouds, we can perform remote sensing with much higher accuracy and apply it to obtain valuable information about the earth and its atmosphere.

Landsat 8 satellite sensor has the capability to detect such high altitude cirrus clouds by viewing the earth through a cirrus band (band 9). One of the main goals of this research is to calibrate the cirrus band in Landsat 8 so that a good estimate of cirrus clouds in any observation can be obtained. By avoiding cirrus clouds in data, accurate information can be obtained.

1.2   Sensor Overview

Remote sensing generally involves a source of energy, the interaction between that energy, atmosphere and earth's surface, and the recording of that energy by the sensor

[4]. In most cases remote sensing instruments are placed either within the atmosphere or above it. Sensors placed on a satellite are an example of an above the atmosphere sensing system. Basically, in passive remote sensing, sensors collect energy that is either emitted directly by the objects viewed or reflected from natural sources like the sun [1]. These types of measured energy collected by sensors depend on its operating wavelength, which is defined by the spectral resolution of the sensor. Sensors can sense energy in multiple spectra with various spectral resolutions; such sensors are known as multispectral sensors [5]. Some sensors can measure energy in hundreds of continuous different narrow spectral bands; such sensors are known as hyperspectral sensors.

Different types of sensors are categorized on the basis of how the image is formed. The simplest imaging sensor is a line scanner, in which a spinning mirror is employed to project the image of a single detector along a line on the ground perpendicular to the satellite ground track. Line scanners often have large fields of view providing greater ground swaths. But line scanner design has a major disadvantage that a single detector does all the sampling, so the dwell time (the time the detector can spend collecting photons from a spot on the ground) is short [1]. Thus due to low dwell time small numbers of photons are collected hence the signal to noise ratio is also small.

Another type of scanning system is called a Whiskbroom. This type of sensor overcomes the short dwell time imposed by the Line scanner by recording several lines of data simultaneously. But they have a disadvantage that they require slightly larger fields of view for the telescope and the spectral data are not inherently registered [1].

The next type of sensor is a Push-broom sensor. It is an advanced type of sensor, which not only increases the dwell time but also increases integration time of the sensor. The push-broom sensor uses a linear array of detectors to record entire lines of data simultaneously [1]. The push-broom types of sensor have the advantage that they don't have any movable parts in satellite operation. This increases the expected lifetime and reduces power requirements. But, this detector technology is more sophisticated than line scanners and whiskbroom scanners. Also, their large focal plane needs cooling which is a difficult task for the designer [1]. Despite these disadvantages, the push-broom sensors are becoming more and more popular in space-based systems because of the advantage of no moving parts, long dwell time that allows for high signal to noise ratio and higher spectral resolution [1]. Fig 1 shows the basics of whiskbroom and push-broom types of sensors.
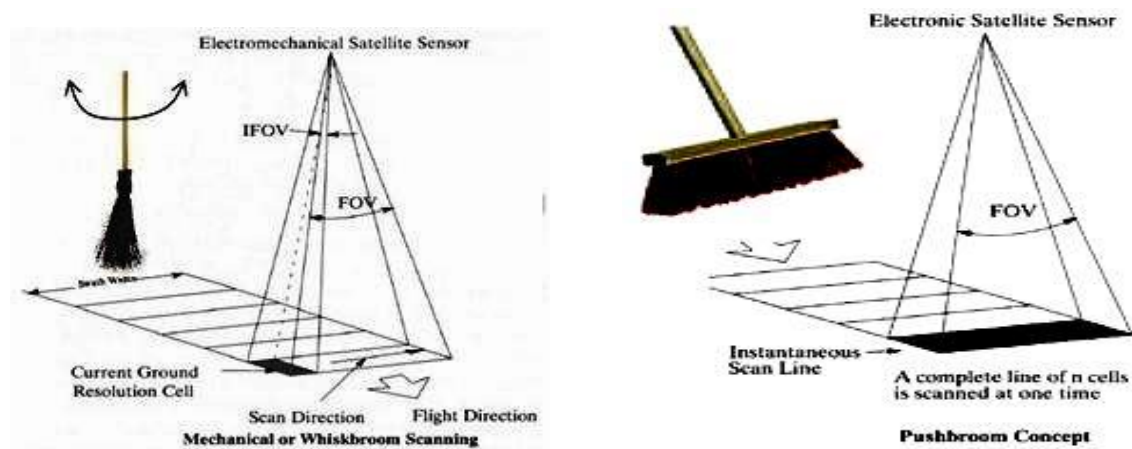
Figure 1: Schematics showing whiskbroom sensor and push-broom sensor [6]**.**

1.2.1   Landsat 8

Landsat satellites have continuously acquired space-based images of the earth's land surface, coastal shallows, and coral reefs since 1972 [7]. The Landsat program is the

joint effort of the U.S. Geological Survey (USGS) and the National Aeronautical and Space Administration (NASA) and was established to routinely gather land imagery from space [7]. Landsat satellites have provided worldwide science and resources management communities with an archive of space-based remotely sensed data of the earth; a valuable resource for the people who work in agriculture, geology, education, regional planning, mapping and global change research.

Landsat 8, launched on Feb 11, 2013, joins Landsat 7 in capturing hundreds of images of the earth's surface each day to ensure continuity of data acquisition to add to the Landsat archive. About 400 scenes are acquired per day by Landsat 8 [7]. The Landsat 8 satellite images the earth every 16 days with 8 day offset from Landsat 7 [8]. Landsat 8 carries two push-broom sensors: The Operational Land Imager (OLI) and Thermal Infrared Sensor (TIRS), both of which provide improved signal to noise ratio and 12 Mbit radiometric quantization of the data [7]. The nominal Landsat 8 altitude is 705 km and it provides a scene size of 185 km cross track by 180 km along track [9].

Figure 2: Landsat 8 [10]**.**

1.2.1.1   Operational Land Imager

The Operational Land Imager onboard the Landsat 8 is a push-broom sensor. It contains four mirrors with a front aperture stop that is 135 mm. The focal plane of OLI is comprised of 14 Focal Plane Modules (FPM) as shown in figure 3.
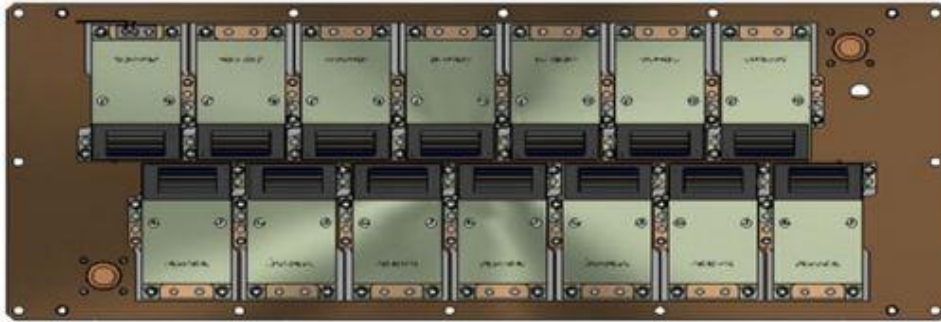
Figure 3: Drawing of OLI focal plane [11]**.**

Figure 3 shows 14 FPMs positioned within the focal plane of OLI. Each FPM contains an array of 494 detectors for each band. There are more than 70,000 detectors in OLI with many additional and redundant detectors continuously observing the earth in different region of the electromagnetic spectrum [**12**]. The staggered fashion of FPM ensures the complete viewing coverage of the field. The spatial resolution of all bands in OLI is 30 m, except for the panchromatic band, which has a spatial resolution of 15m; also the pan band has twice the number of detectors as compared to the other bands. The spectral filter on the top of each FPM ensures that each band is irradiated by its corresponding wavelength of light. The detectors for visible light are a silicon based compound as they have suitable energy band gap for the visible electromagnetic spectrum. The detectors that detect longer wavelength are made up of HgCdTe compound, which is suitable for detection of the electromagnetic spectrum at longer wavelengths. The detectors in OLI give an output of 14 bit Digital Number (DN). Out of

this 14 bit data only 12 Most Significant Bits (MSB) are recorded and transmitted to the ground and the lower two Least Significant Bits (LSB) are ignored except for some calibration data collection [**13**].

OLI provides both internal calibration sources, such as lamps, for radiometric stability and it have the capabilities to perform solar and lunar calibrations as well. OLI can collect the energy in nine different wavelengths of electromagnetic radiation. Table 1 shows spectral ranges of the OLI bands [**12**].
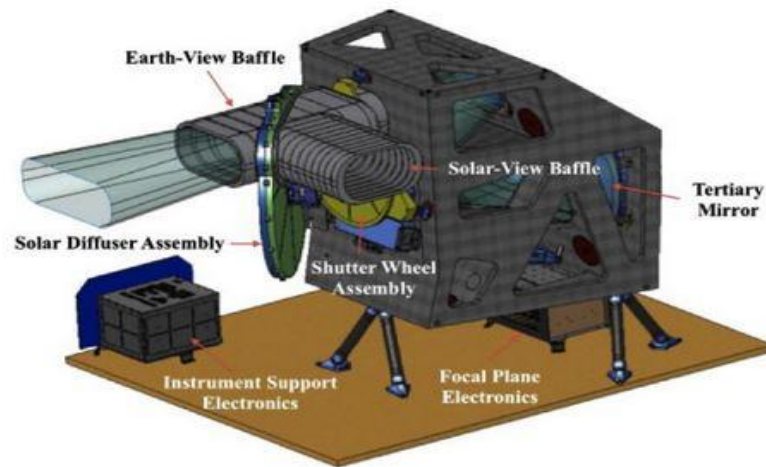
Figure 4: Drawing of Operational Land Imager [11]**.**

Table 1: Spectral ranges and pixel sizes of OLI bands [12].

#	Band Center	Wavelength (nm)	Center Wavelength Tolerance (±nm)	Minimum Lower Band Edge (nm)	Maximum Upper Band Edge (nm)
1	Coastal Aerosol	443	2	433	453
2	Blue	482	5	450	515
3	Green	562	5	525	600
4	Red	655	5	630	680
5	NIR	865	5	845	885
6	SWIR1	1610	10	1560	1660
7	SWIR2	2200	10	2100	2300
8	Panchromatic	590	10	500	680
9	Cirrus	1375	5	1360	1390

1.2.1.1.1 Cirrus Band

The OLI cirrus band is unique to the Landsat series. This band has a ground sampling distance of 30 m and it is centered at 1375 nm with lower band edge at 1360 nm and upper band edge at 1390 nm. The cirrus band observes the earth in shortwave infrared region of spectrum band. At this wavelength, signals from the earth's surface do not reach the sensor because the water vapor in the atmosphere absorbs the signal at this frequency. Because of the strong absorption by water vapor and carbon dioxide, no radiation reflected by the surface of low and mid-level clouds, except for the clouds higher than 6 km, is detected by the cirrus band [14].

Cirrus clouds are typically located at altitudes above 6 km in Artic regions, 7 km in Mid-Latitude regions, and 9 km in Tropical regions, which are above 90-99% of atmospheric water vapor [14]. Cirrus clouds appear bright while most land surface appears dark

through the cloud free atmosphere containing water vapor [3]. Hence the cirrus band is designed to see not land but the high altitude clouds which are not otherwise visible in other bands.

One of the major challenges the cirrus band has shown is its calibration. Since its operating spectrum lies at the water vapor absorption band in the earth atmosphere, it does not sense any signal from earth targets. Hence, it is difficult to calibrate it using standard vicarious calibration methods or any other methods based on observation of earth targets.

1.2.1.2   Thermal Infrared Sensors (TIRS)

The Thermal Infrared Sensor (TIRS) is another instrument onboard Landsat 8. It images the earth in two infrared wavelengths 10.8 and 12 microns respectively [12]. The bandwidth of these bands is significantly larger than that of OLI bands with a coarser spatial resolution of 100 meters. This design constraint is expected because the energy radiated in this spectrum by the earth is very small.

The TIRS operates in push-broom method and achieves the swath width of 188 km. Later the 100 meter resolution is resampled to 30 meters for final image product. The focal plane array is comprised of sensor chip assemblies with a quantum well infrared photometer (QWIPS). The FPMs (Focal Plane Module) are cyro-cooled to 43 K and the optical assembly is cooled to 180 K passively. TIRS can be calibrated using a variable temperature blackbody or space views [12]. Figure 5 shows the schematics of TIRS in Landsat 8 and its focal plane module showing QWIPS detectors.
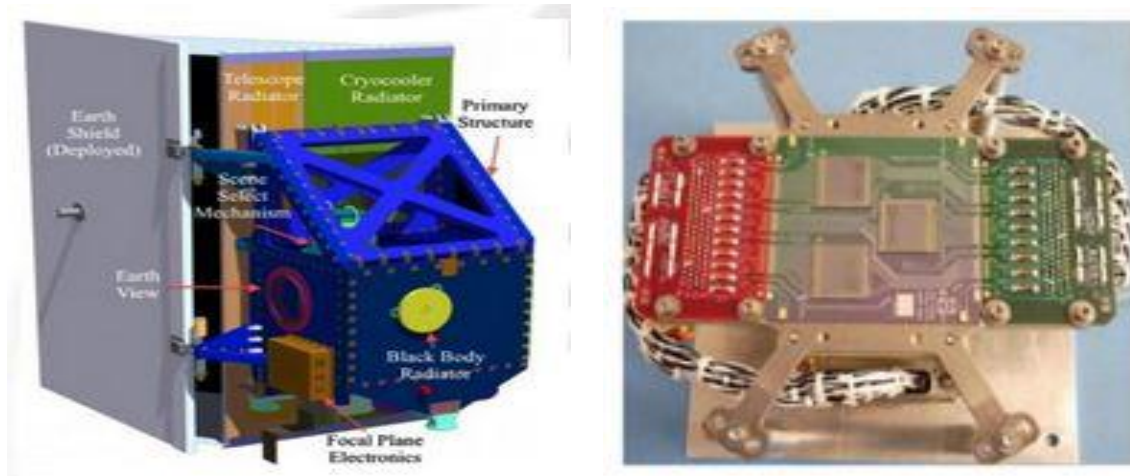
Figure 5: Drawing of the Thermal Infrared Sensor (Left) and Drawing of TIRS focal plane (right).

1.2.2   SCIAMACHY on ENVISAT

The Scanning Imaging Absorption Spectrometer for Atmospheric Cartography (SCIAMACHY) is a passive remote sensing instrument that observes the backscattered, reflected, transmitted or emitted radiation from the atmosphere and earth's surface in different wavelengths ranging from 240 nm to 2380 nm. The SCIAMACHY hyper-spectral instrument was launched onboard the Envisat satellite on March 1, 2001, by European Space Agency (ESA) [15]. It is not operational now and stopped responding on April 8, 2012. SCIAMACHY instrument provides spectra measured from light transmitted, back scattered or reflected by trace gases in the atmosphere. The Envisat satellite was in a 10 AM sun-synchronous orbit with a 35-day repeat cycle at an altitude of 790 km.

Primarily, SCIAMACHY measures various traces of gases in the troposphere and stratosphere which are retrieved from traces of irradiance and earth radiance spectra.

SCIAMACHY makes spectral measurements in passive limb and nadir looking spectrometer observations to permit ground-based computation of trace constituent concentrations [16]. The measurements obtained from SCIAMACHY helps us to investigate a wide range of phenomena which influence atmospheric chemistry such as measurements in the troposphere, biomass burning, pollution, artic haze, forest fire, ozone chemistry, cloud chemistry, volcanic chemistry and solar proton events [17].

The SCIAMACHY products are classified as Level 0, and 1B. SCIAMACHY Level 0 is composed of time ordered and annotated in instrument data units which contain a main and specific product. The SCIAMACHY level 0 product is the basis of all data processing to create other higher level SCIAMACHY product [16]. SCIAMACHY Level 1B products are geolocated spectra, radiometrically and spectrally calibrated radiance for nadir, limb, and sun/moon occulation geometries [16].Based on nadir scans of SCIAMACHY (Level-1B version-7.03), DCC reflectance spectra were obtained by Dr. Doelling and his team at Langley Research Center, National Aeronautics and Space Administration, Hampton, VA.

1.3   Sensor Calibration

Calibration is a set of operations that under certain conditions establish the relation between values indicated by a measuring instrument and values realized by measurement standards [18]. The Working Group on Calibration and Validation (WGCV) of the International Committee on Earth Observation Satellites (CEOS) has defined remote sensing calibration as the process of quantitatively defining the system response to known controlled signal inputs. Thus, the data extracted from satellite images are digital

numbers (DNs) and they do not directly provide any physical or radiometric information. To extract real physical or radiometrical information from those image's digital numbers, transformation is required; this transformation is known as calibration. To perform analysis such as investigating the temporal stability of the sensor, the radiometric calibration is necessary. The radiometric calibration of the sensors on the Landsat series of satellites is the contributing factor for the success of the Landsat dataset [19].

Calibration and validation is an important aspect of any remote sensing system. The calibration of Landsat 8 sensors is supported by data from preflight, post-launch, onboard, and ground reference [20]. The Calibration Parameter File (CPF) provides radiometric and geometric coefficients needed for processing raw, uncorrected images. Calibration of sensor helps to characterize the operation of sensor and also provides quantitative sense to sensor data.

1.3.1   Absolute Radiometric Calibration

Absolute calibration is the process that converts the voltage recorded by the satellite sensor or digitized counts to absolute radiance units [21]. The calibration of the satellite sensor can change with time due to various phenomena such as outgassing, variation in filter transmittance and spectral response and slow deterioration of sensor electronics, etc. Thus, absolute calibration is necessary to characterize and assess the performance throughout a sensor's lifetime from prelaunch to on-orbit operations, so that radiometrically accurate data can be provided to the user community [21]. During prelaunch calibration, a series of elements are calibrated and characterized which includes optical sensors, optical path components and onboard calibrators, such as lamps,

blackbodies and reflectance panels [21]. Post launch calibration includes different techniques such as measurement of on board calibrators, vicarious calibration, cross calibration between different satellite sensors, and use of lunar and stellar sources etc. Radiometric characterization is a prerequisite for creating high-quality science data, and consequently, higher level downstream products [22].

Table 2: Hypothetical calibration response curve.
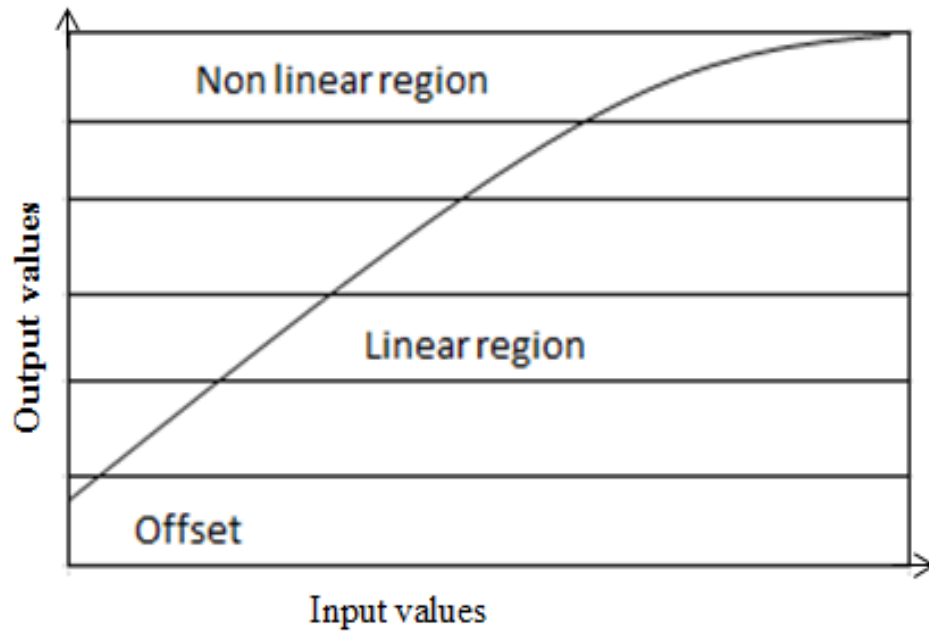
Above is a hypothetical calibration response curve to a known signal. For each spectral band, the digital number (DN) output from the sensor system is related to radiance by the following equations.

$$DN = G * l + B$$

$$l = (DN - B)/G$$

The sensor's gain, G, and bias, b, from the above equation can be used to convert sensor data (DN) to physical units; radiance or reflectance as required. The above equation is valid in the linear operation region of the sensor.

1.3.2   Relative Radiometric Calibration

Ideally, every detector in an imaging sensor made out of the same bulk material would possess an identical response to a given incident radiance level. However, detectors and amplifiers in most imaging systems exhibit varying degrees of unequal response, which often results in noticeable striping in the imagery [23]. Relative radiometric calibration involves removing such prevailing stripes due to unequal detector responses in satellite imagery. Figure 6 shows radiometrically uncorrected image from the cirrus band image from Landsat 8. There are many visible stripes which occurred due to a slight difference in detector responses.
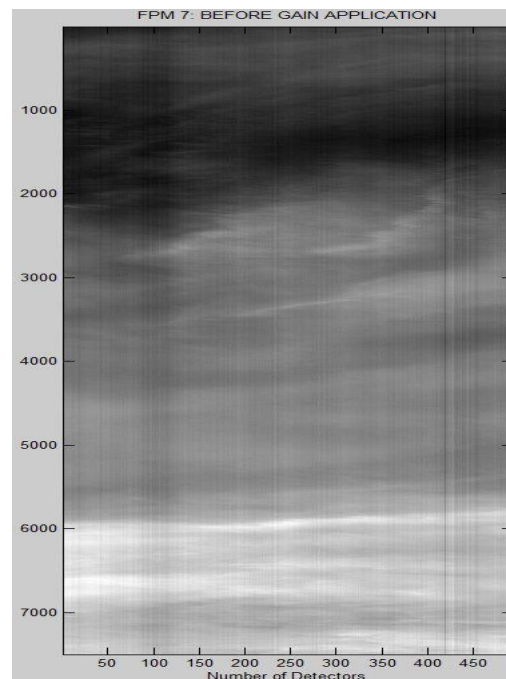
Figure 6: Radiometrically uncorrected cirrus band image (FPM 7).

Various methods have been developed to perform relative radiometric calibration under the assumption of linear detector responses. There are mainly two major categories 1) those that rely on internal calibration data and 2) those that rely on using image data [4]. The calibration based on internal calibration involves the use of internal calibration lamps or solar panels. The detectors are exposed to calibration lamps or solar panels and the responses from each detector are recorded. The recorded data is used to estimate gain and bias for each detector. Calibration based on scene statistics uses the histogram equalization method. In this method, relative gain is estimated from first and second order statistics obtained from image data; these gains can be calculated with respect to an individual reference detector or the average of all operative detectors. This method works for whiskbroom types of sensor but for push-broom sensors, such as Landsat 8, this method doesn't work because a detector at one end of an array does not measures an identical radiance level as the detector at the other end of the array. Thus a statistical approach is applied for push-broom sensors where relative gain is estimated by averaging the composite detector statistic obtained from a large number of images [23].

1.4   Thesis Overview

The major goal of this thesis is to develop a method for absolute radiometric calibration of cirrus band and coastal aerosol band and relative gain analysis of cirrus band based on Deep Convective Cloud (DCC) imagery. Very cold and highly reflective DCCs are used for the development of a calibration algorithm. For this method, Landsat 8 imagery was used and the calibration was transferred from well-calibrated reflective bands (band 2, 3, 4, 5) of Landsat 8 to cirrus band and coastal aerosol band using DCC spectra from SCIAMACHY as a transfer medium.

The absolute and relative calibration work can be summarized as follows.

Absolute gain

- Use scene mean characteristics of reflective, thermal and cirrus band to find Deep Convective Cloud images from Landsat 8 archive.

- Obtain DCC pixels and find their reflectance and radiance using standard conversion equations.

- Determine the gain of Cirrus band and Coastal aerosol band using band to band calibration of reflective bands and SCIAMACHY DCC spectra.

Relative gains

- Use scene mean characteristics of reflective, thermal and cirrus band to find Deep Convective Cloud images from Landsat 8 archive.

- Obtain detector level statistics for selected scenes and derive relative gains from it.

- Apply DCC derived gain to L1Rp scenes (geometrically corrected, bias removed, gain unapplied scenes).

- Compare the results by using streaking metric for both DCC gain applied scenes and default gain applied scenes.

Description about previous work on absolute and relative gain, and a brief description about SCIAMACHY DCC spectra and its acquisition procedure can be found in chapter 2 along with a description of the Landsat 8 Cal/VAL algorithm development document.

A thorough description about the location of DCC scenes, obtaining reflectance, radiance of DCC pixels and use of SCIAMACHY DCC spectra to determine absolute gain for

cirrus band and coastal aerosol band in Landsat 8 can be found in chapter 3. Similarly, a description of the procedure used for relative gain derivation and its analysis can be found in chapter 4. Chapter 5 summarizes all the results of relative gains and absolute gain obtained from DCC imagery. Finally, conclusions obtained after this work was accomplished and recommendations for future work are also described in this chapter.

CHAPTER 2

2   LITREATURE REVIEW

2.1   Landsat 8 CAL/VAL Algorithm Description Document (ADD)

The document is a guide to the overview of the instruments and their data followed by discussion of the design philosophy, data flow diagram and algorithm descriptions developed within the Cal/Val Toolkit for geometric and radiometric characterization and calibration [12].

The Landsat 8 CAL/VAL Algorithm Description Document was useful throughout the research to understand Landsat 8 sensors, different bands in OLI, different bands in TIRS and to understand the processing flow of the data during image processing. It helped to understand the parameter given in the Calibration Parameter Files and Bias Parameter Files. Similarly, these documents gave detailed insight and help to understand detector level data as well as the final data product (L1T). The description about staggered array design of OLI, number of detectors in each band, orientation and properties of each FPMs, was helpful to determine relative gain of the cirrus band.

2.2   LDCM level 1(L1) Data Format Control Book (Version 6.0)

The Data Format Control Book (DFCB) establishes the data format for LDCM level 1 product [24]. Detailed information about LDCM L1GT/L1T output data file format and packaging can be obtained from it. The Level 1 product consists of the following:

- The Level 1 Systematic Terrain Corrected (L1Gt) product created using Digital Elevation Models (DEMs) and ephemeris.

- The Level 1 Terrain (corrected) (L1T) precision corrected product created using ground control points, DEMs, and ephemeris.

This document was mainly helpful in research to understand the naming convention associated with Level 1 products of Landsat 8. It also defines different data formats and their storage format. This document helps to extract valuable information from Landsat8 data products. Some of the data products that were used in this research are as follows.

- Level 1R (L1R) data product – L1R data products consist of radiometrically corrected data from image data with all data transmission and formatting artifacts removed [24].
- Level 1 Terrain corrected (L1T) – L1T data products consists of L1R with systematic geometric corrections applied, using ground control points or onboard positional information [24].

2.3   Deep Convective Clouds (DCCs)

DCCs are mainly defined as highly convective clouds over the Tropical Tropopause Layer (TTL) [25]. When strong convective clouds overshoot the TTL extending from 14 to 19 Km, the temperature of the up-drafting air decreases continuously with the upward motion, followed by near-dry adiabatic (a process in which there is no heat transfer between system and surrounding) because of very small amounts of water vapor in the air, this results in a cloud top temperature lower than the tropopause temperature [25]. DCC can be identified by using a brightness temperature threshold [26]. For example, Zipser et al. used BT<210K, B-J. Sohn et al. used BT<190 K, Doelling et al used BT<205K to detect DCCs [25] [27]. Many researchers have used

other cloud data, such as cloud optical thickness, cloud height, effective particle size and cloud temperature, to detect DCCs.

Deep Convective Clouds (DCCs) are very bright, and nearly isotropic solar reflectors located over the tropics and they can be easily identified using the simple infrared threshold [27].They have the highest signal to noise ratio of any earth target, and are near Lambertian reflector under non oblique viewing and illumination conditions, thus they are ideal visible calibration targets. They are located at the tropopause where the radiative impact of atmospheric water vapor absorption, aerosol, and surface albedo is minimal. Thus, they exhibit a nearly flat spectral response [27]. There are three dominant DCC domains where the frequency of the DCC occurrence is highest: The Tropical Western Pacific (TWP), Equatorial Africa, and South America region. These regions are shown in Figure 7. DCCs can be found in these regions round the year. Hu et al, Doelling et al, Aumann et al, Minnis et al and many other scientific groups have studied and used DCC for calibration of Geostationary satellites [27] [28] [25] [29].
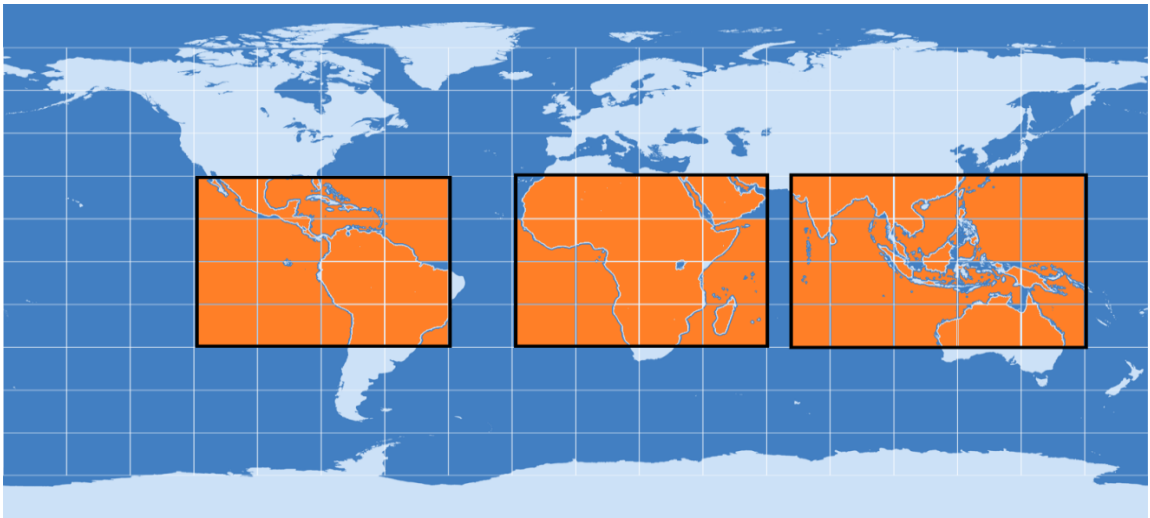
Figure 7 : A world map showing three main DCC domains (yellow regions) between 30 N and 30 S [27] [30]**.**

2.4   Previous Work in DCCs as Calibration Targets

Hu et al. pioneered the calibration technique using DCC and used DCC pixel level radiance over months [29]. They evaluated the stability of the clouds and the Earth Energy System Broadband (BB) Shortwave Fluxes and Visible Infrared Scanner (VIRS) and MODIS visible radiances on board the Tropical Rainfall Measuring Mission (TRMM) and Terra satellites respectively [29]. Using a similar technique, Doelling et al. used a simple IR threshold and CERES DCC BB bidirectional reflectance distribution function (BRDF) to determine relative temporal degradation of AVHRR on board NOAA 16 and NOAA 17 satellites [27].

Youngxiang Hu et al. used cloud-top temperature less than 205 K and optical depth (optical depth measures how transparent a cloud is or how much the cloud modifies light passing through it) greater than 40 to find cold opaque deep convective clouds, and they performed a monthly deep convective cloud planetary albedo distribution from broadband observation using the CERES instrument on TRMM [29]. Aisheng Wu et al. observed the temporal trends for two wavelength bands (0.47 micron and 0.55 micron) of Terra MODIS [31]. The comparison of results of those bands with the trends obtained from well understood deserts agrees with the trend obtained by DCC observations [31].

Doelling et al. showed that Deep Convective Clouds are ideal visible calibration targets as they are bright, nearly isotropic solar reflectors located over the tropics and can be easily identified using a simple infrared threshold [27]. DCCs are ideal invariant Earth targets as they are the brightest calibration targets. They are common in the tropics and migrate seasonally with the sun, thus they are optimal solar reflectors [27]. DCCs have

the highest signal to noise ratio of any earth targets. They are nearly isotropic under a non-oblique viewing and illumination angle. They are located in the tropopause where the radiative impact of atmospheric water vapor absorption, aerosols and surface albedo is minimal [27].

Doelling et al. have developed a DCC calibration technique (DCCT) which is a two-step process. In this technique, any pixel located over the tropical domain between 30^oN and 30^oS with an 11micron Brightness Temperature (BT) less than 205 K is identified as a DCC pixel target. To capture only the convective core of such clouds, a spatial uniformity threshold is applied by computing the spatial standard deviation of the identified pixel and its eight surrounding neighbors. Pixels with standard deviation less than 3% in visible and 1Kelvin (K) in the IR are used. Solar zenith angles and view zenith angles less than 40° are only used to take advantage of the Lambertian part of the DCC reflectance field. Finally anisotropic correction is applied to the DCC radiance and sensor temporal stability is analyzed [27].

2.5   Previous Work in Relative Radiometric Gains

Relative radiometric calibration can be grouped into two major categories: those that rely primarily on internal calibration data and those that rely on image data [32].

Relative radiometric calibration methods were compared for the Landsat Multispectral Scanner Subsystem (MSS) in 1993 by Helder [32]. The MSS in Landsat 1 through Landsat 5 was a whiskbroom sensor. Their paper compares relative radiometric calibrations based on internal calibration data and calibration based on scene statistics. It suggested that calibration of MSS data using the scene statistics approach is more

effective although both methods have few drawbacks. Helder et al. characterized the relative gain of Landsat 5 Thematic mapper (TM) for six reflective bands [33].

Initial work for relative gain characterization for pushbroom sensors such as ALI was done by Angal in 2005 [23]. This paper estimated the relative gains for each of ALI's bands based on the histogram equalization approach using statistics from 4993 scenes and it was concluded that the gain estimates based on lifetime scene statistics performed as well as and in many cases better than estimates based on pre-launch calibration coefficients [23].

Another method to derive relative gains for a push-broom sensor is using a 90° Yaw Maneuver or Side Slither Maneuver. This method for Landsat 8 is being developed at SDSU image processing lab and other labs. The basic idea of this method is to use a single image to calculate relative gains; but, for this method the sensor platform is rotated by 90° and is parallel to the direction of platform motion. Thus it allows all the detectors to measure the same radiance levels from the same target as it moves in its orbit. However, for the staggered push-broom detector array configuration of OLI in Landsat 8, this method has to be modified [34]. The FPM's on OLI are staggered within the focal plane array and even and odd FPMs will observe a different target even in the side–slither maneuver. Also the detectors within the FPAs are also staggered so while calculating gains all these design constraints care should be taken [34]. Helder et al. showed that for visible/near infrared (VNIR) bands on OLI, side slither sites with the highest spectral radiance are those over snow-covered regions, such as Greenland and Dome C of Antarctica, whereas for the SWIR band, Saharan desert sites are good for relative gain characterization [34].

The cirrus band in Landsat 8 operates on the water vapor absorption band so it is difficult to calibrate this band using the methods above. Thus for the first time, Deep Convective Clouds are investigated for the characterization of relative gains. DCC extends high up to an altitude of 14 km to 19 km in the tropopause layer [25]. At this height the effect of atmospheric water vapor absorption, aerosol, and ozone effect is minimal [27]. DCC has a very high signal to noise ratio. Because of these characteristics, DCCs are ideal earth targets to characterize relative gains for cirrus bands in Landsat 8.

CHAPTER 3

3   ABSOLUTE GAIN DERIVATION FOR CIRRUS BAND AND COASTAL

AEROSOL BAND USING DCC AS INTER-BAND CALIBRATION SOURCE

3.1   Algorithm Development

As previously mentioned, DCCs are being used to calibrate different satellite

sensors. Doelling et al. developed a baseline DCC technique for the GOES satellites [27].

In that technique, any pixels located over the tropical domain between $30^{o}N$ and $30^{o}S$

with an 11 micron BT less than 205K was identified as DCC pixel target [27]. Spatial

homogeneity thresholds were further used to capture only the convective core of DCC.

Most of the published previous works on DCC calibration are focused on calibration of

GOES satellites with large spatial resolution. Also most of the previous works were

focused on the calibration of solar reflective bands. This research work is carried out to

explore the use of DCC calibration technique for calibration of cirrus and the coastal

aerosol bands in moderate resolution sensors like Landsat 8.

The basic idea behind this research work is to identify DCCs for moderate

resolution sensors like Landsat 8 and to transfer the calibration of well-calibrated

reflective channels of Landsat 8 to cirrus and coastal aerosol bands using DCC

SCIAMACHY spectra as a calibration transfer medium. Thus, initially, DCCs need to be

identified from the Landsat 8 image archive.

3.1.1   Search for DCC Scenes

The frequency of DCC is high in the Tropical Western Pacific region, South

America region and Africa region. Small sun angle is required to take advantage of the

Lambertian property of DCC. Initially, the scene statistics for all the Landsat 8 scenes between 30° N and 30° S from six consecutive months (May 2013 to October 2013) were obtained from USGS archive using the Image Assessment System (IAS) (IAS is a special system designed to handle all the processing related task of Landsat 8 imagery). The scene statistics contains: scene ID, scene mean DN for all the bands, scene latitude, longitude, time and date of scene acquisition and sun angle information.

As previously mentioned, DCCs are very cold and highly reflective clouds, so the scenes which contain a large number of DCC pixels must have a very low scene mean brightness temperature and very high scene mean radiance for reflective bands. This basic idea was used to narrow down the search for DCC scenes from the pool of selected Landsat 8 scenes within 30° N and 30° S latitude.

3.1.2   Thresholds for Identifying Scenes with DCC Pixels

In this work, Landsat 8 band 4, band 10, and band 9 were used to identify DCC scenes. Figure 8 shows the plot of brightness temperature (band 10), radiance (band4) and radiance (band9) for the month of May 2013. The selected scenes were then sorted from low to high based on mean BT as shown in Figure 8.
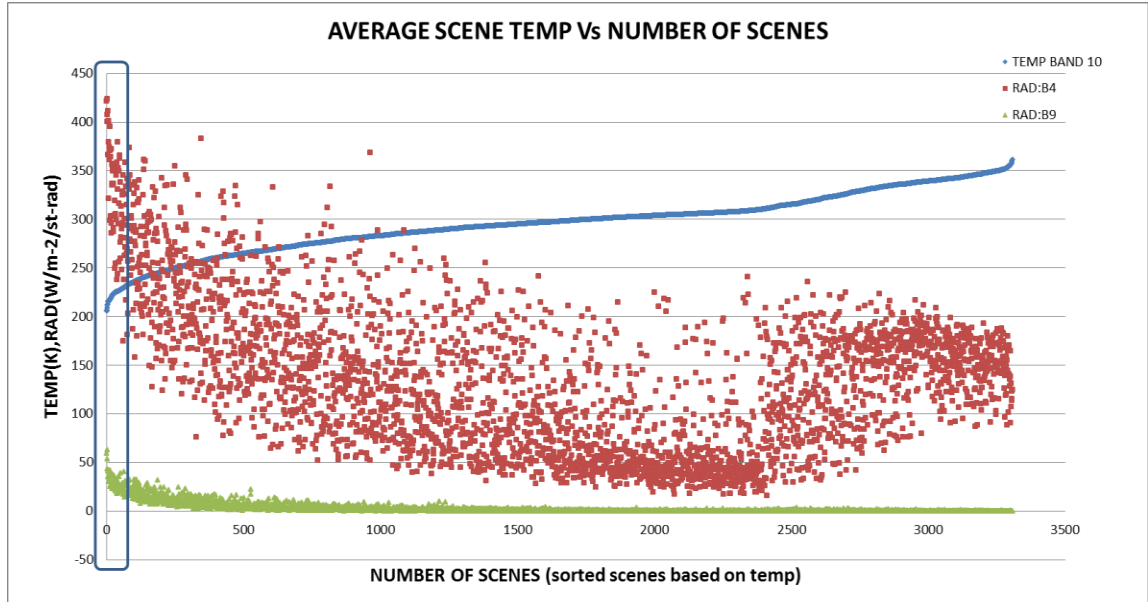
Figure 8: Scenes sorted on the basis of temperature to select DCC scenes.

The corresponding scene mean radiance for band 4 and band 9 for corresponding scenes was also plotted. The plots for each month were analyzed. At mean brightness temperature below 250 K, an identifiable switch over from DCC to non-DCC can be observed. The scenes below 250K mean BT has high scene radiance in band 4 and in band 9 as well. Thus they represent the cold and bright cloud containing scenes in the tropopause. Based on these observations thresholds were set and DCC containing scenes were selected from the Landsat8 archive and passed on for further processing.

Thus, based on the above analysis, the scenes between 30°N and 30°S, having scene mean BT (10.8 micron) less than 250K, scene mean radiance (0.655 micron) greater than 250 watts m^{-2} sr^{-1}, scenes mean radiance (1375 nm) greater than 10 watts m^{-2} sr^{-1}, are identified as scenes containing DCC pixels, these scenes and used for further analysis.

Scene mean brightness temperature represents the mean of all the detector responses, thus we can easily assume that, scenes meeting the above criteria potentially have DCCs somewhere in the scene. The mean radiance threshold of greater than 250 watts m^{-2} in band 4 (0.655 micron) ensures that very bright targets only are selected. The scene mean radiance of greater than 10 watts m^{-2} sr^{-1}in band 9 ensures that very high altitude bright targets only are selected. Similarly, scene mean temperature less than 250 K, also removes the false identification of bright and hot sites like deserts. So the combination of these criteria did a good initial job of removing non-DCC images. Using the above mentioned procedure, a total of 154 scenes from 6 months (June 2013 to October 2013) were selected and further analyzed.

3.1.3   Inter-Scene DCC Pixel Identification

After the preliminary selection of scenes, they are downloaded into the archive at SDSU. To quantify how many DCC pixels were present in each scene and to find the radiance, reflectance and brightness temperature of each DCC pixel, pixel by pixel analysis of each scene was performed. DCC pixels were selected on the basis of brightness temperature thresholds, and to capture the homogenous convective core of cloud, spatial homogeneity thresholds were applied.

3.1.3.1   Brightness Temperature Threshold

Brightness temperature threshold was the major criteria in identifying DCC pixels in a scene. Zipser et al. used a BT less than 210 K to identify DCCs. Doelling et al. used a brightness temperature (11 micron) less than 205K to identify a DCC pixel [27]. Their work was for the GOES sensors with large pixel size such as 1Km by 1Km. For the

sensors with a much smaller GSD such as 30 m for Landsat8, modification in DCC

detection needs to be done. For example, if a DCC cloud is observed by GOES sensor

and same DCC is observed by Landsat 8, the GOES scene will have few DCC pixels

whereas for Landsat scene there will be a large number of DCC pixels.

The lower BT targets the coldest and cleanest DCCs that lie in the core of clouds.

The surrounding of the DCC core is called anvils of clouds. These anvils are also cold to

be detected in IR threshold as DCC but they should be avoided to obtain uniform DCC

pixels. Initially BT<205K was used to analyze DCC pixels in each scene. A DCC scene

when applied with BT<205K and spatial homogeneity thresholds is shown in Figure 9.

The frequency of DCC pixels in each scene can be seen in the Probability Density

Function (PDF) shown in figure 10.
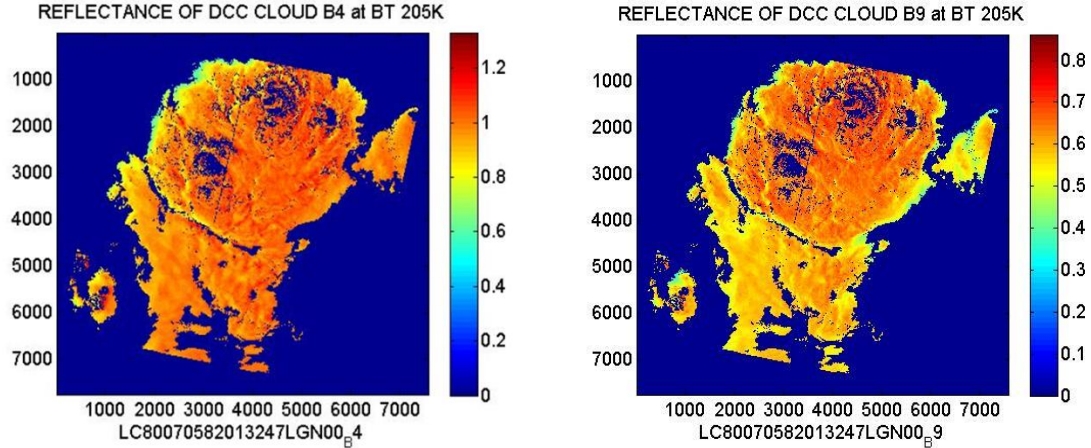
Figure 9: DCC pixels detected, when BT threshold < 205K was used (left: band 4, right: band 9) (DCC count: 20,076,783 pixels).

Figure 9: shows DCC pixels of the scene (LC80070582013247LGN00), when the

brightness temperature threshold<205 K is used and spatial homogeneity thresholds are

applied. Band 4 scenes shows uniform reflectance throughout the entire DCC region,

whereas the cirrus band scene shows two different features, one with higher brightness

and the other with lower. This feature is clearly seen in normalized Probability Density

Function (PDF) of each scene in Figure10. Figure 10 (left) is the PDF of the DCC

reflectance in red band. It has almost normal shape. The single peaked PDF represents a

uniform DCC pixel region. Figure10 (right) is the PDF of the DCC reflectance in cirrus

band. There are two peaks in the PDF suggesting two different types of reflectance values

present in the scene.
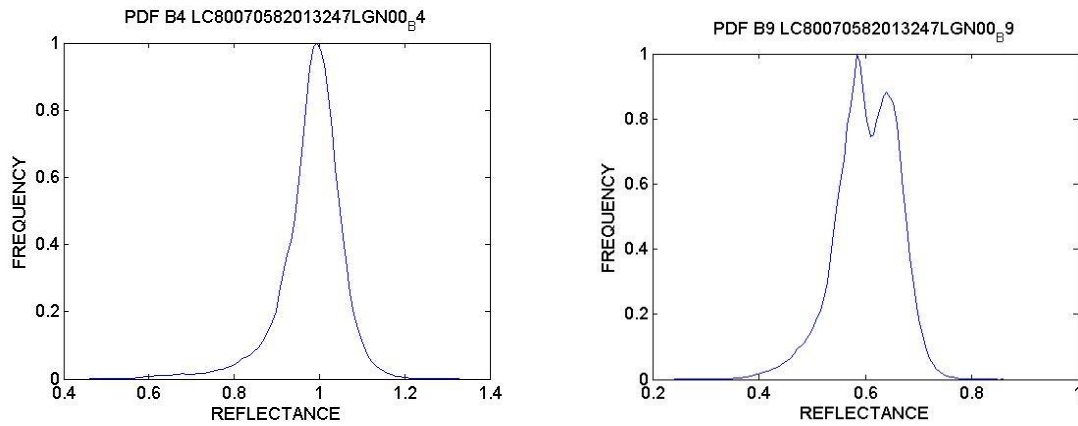
Figure 10: Normalized PDF of the same scene as shown in figure 10 (BT threshold < 205K) (left: band 4, right: band 9).

To remove such non uniform pixels from the scene, threshold BT<195K was used

and analyzed. Figure 12 shows DCC pixels of same scene (LC80070582013247LGN00)

as in Figure 10, when BT<195 K.
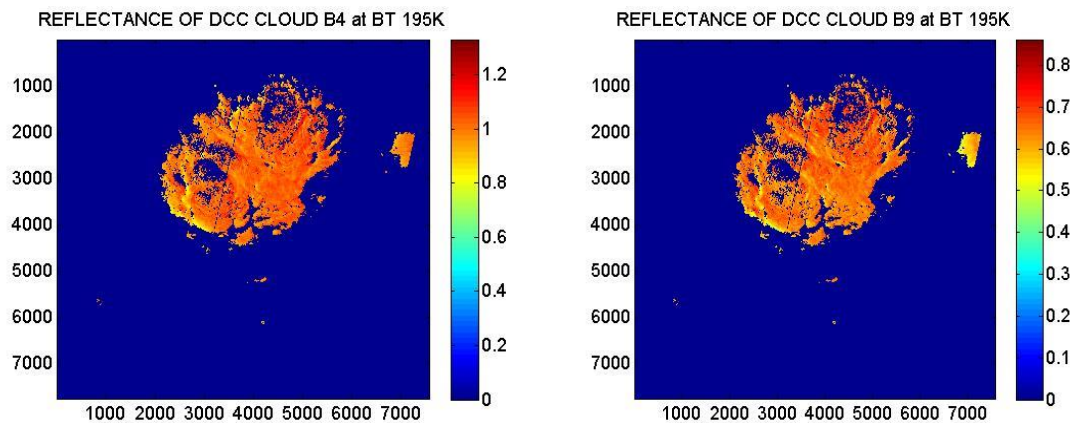
Figure 11: DCC pixels (6,846,444 pixels) detected when BT threshold < 195K is used (left: band 4, right: band 9).

When 195 K is used as threshold, cirrus and red band both are showing uniform reflectance. The PDF in Figure 12 shows similar shape both in cirrus and red band. Both PDFs in Figure13 (left and right) have a single peak suggesting that scene contains DCC pixels with uniform reflectance.
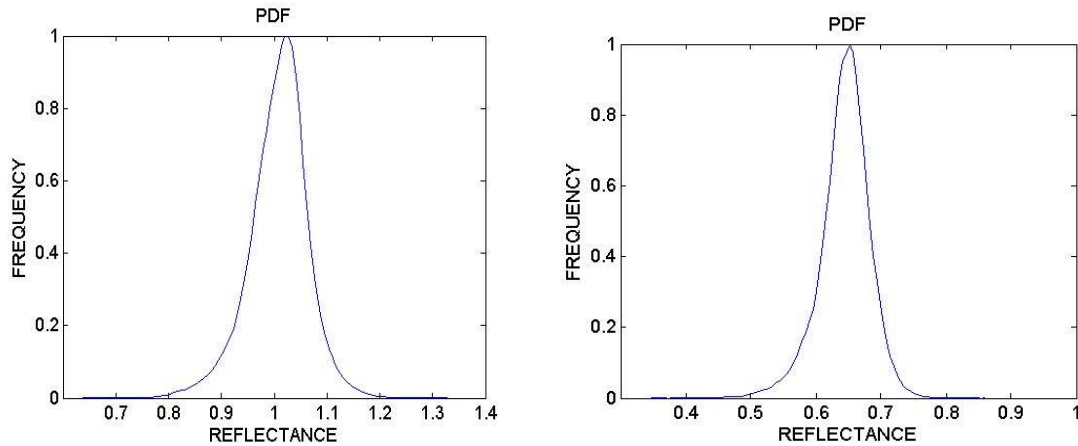
Figure 12: PDF of the same scene as shown in figure 12 (BT threshold < 195K) (left: band 4, right: band 9) (DCC count: 6,846,444 pixels).

Thus, it can be seen that the colder temperature threshold targets the colder and purer (pristine) DCCs that produce a uniform PDF in both reflective and cirrus band. This coldest core of the clouds represents purer deep convective clouds [**27**], thus based on extensive research, the brightness temperature threshold of 195K is used.

3.1.4   Spatial Homogeneity Threshold

DCCs have cold anvils (clouds surrounding the core) surrounding the cold core of the cloud. Only the center of such cloud represents the deep convection [**27**]. There can be non-uniform clouds pixels around a DCC pixel. So, to capture the core of such cloud and remove non uniform cloud pixels, spatial homogeneity threshold is applied. The spatial homogeneity threshold is obtained by analyzing each and every pixel with respect

to its surrounding. Homogeneity threshold was devised by taking a 15x15 matrix of pixels in DCC scene and analyzing the central pixel with respect to its surrounding pixels. If the central cloud pixel (shown by red pixel in Figure 14) surrounded by 225 pixels, in a 15 by 15 pixel matrix has BT (10.8 micron) <195K, and has standard deviation in brightness temperature (10.8 micron) less than 1K with respect to surrounding 225 pixels and has standard deviation in radiance of red band (0.655 micron) less than 3% with respect to surrounding 225 pixels, then that pixel is identified as DCC pixel. This method is applied through the entire scene for each and every pixel and uniform DCC pixels are collected.
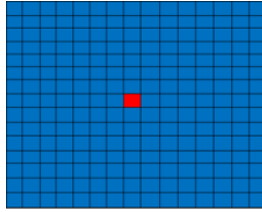
Figure 13: 15x15 pixel matrix for spatial homogeneity. If the central pixel has standard deviation of less than 1K in band 10 and less than 3% in red band with respect to surrounding pixels then it was chosen as DCC pixel.

3.1.5   Analyzing DCC Pixels

After identifying uniform DCC pixels from each scene, the DN value of each DCC pixel is converted to TOA reflectance for each using the following relations respectively.

$$L_\lambda \ = M_l \, Qcal + A_l \quad [\mathbf{35}]$$

Where,

L_λ = TOA spectral radiance (watts m^{-2} sr^{-1})

M_l = band specific multiplicative rescaling factor from the metadata file

A_l = band specific additive rescaling factor from the metadata file

Q*cal* = quantized and calibrated standard product pixel values (DN)

$$\rho_\lambda = M_\rho Qcal + A_\rho \quad [\mathbf{35}]$$

Where,

ρ_λ = TOA reflectance, without correction for solar angle

M_ρ = band specific multiplicative rescaling factor from the metadata file

A_ρ = band specific additive rescaling factor from the metadata file

Qcal = quantized and calibrated standard product pixel values (DN)

$$T = \frac{K_2}{\ln\left(\frac{K_1}{L_\lambda}\right)+1} \quad [\mathbf{35}]$$

Where,

T = at sensor Brightness temperature (K)

L_λ = TOA spectral radiance (watts m^{-2} sr^{-1})

K_1 = band specific thermal conversion constant from the metadata

K_2 = band specific thermal conversion constant from the metadata

For each scene the DCC pixel count, along with mean reflectance, mode of reflectance,

standard deviation in reflectance, and probability density function for each band was

obtained. A typical cold and bright cloud scene with deep convection is shown in Figure 14.
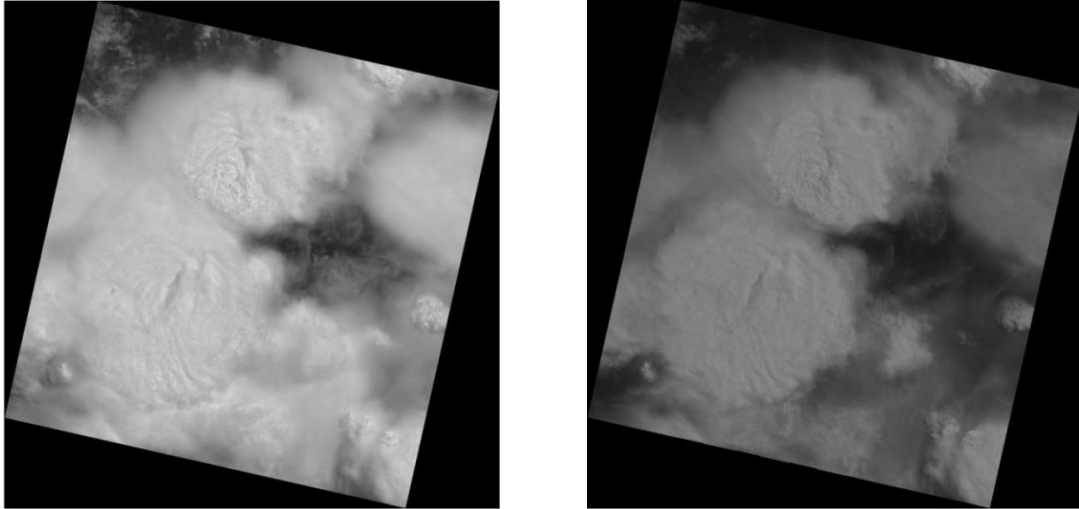
Figure 14: A DCC scene in red band (left) and in cirrus band (right).

A cold and bright cloud scene can be seen bright in Figure 14. The band 4 scene (image left) was observed brighter the than band 9 scene (right). After applying thresholds DCC region was obtained for the above Landsat scene which is shown in Figure 15.
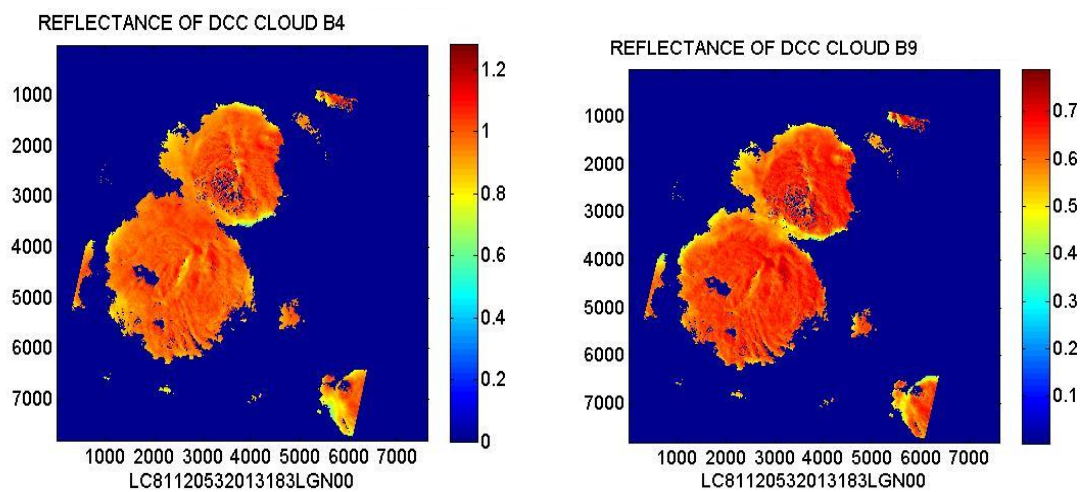
Figure 15: DCC scene after analysis, showing the DCC pixels (red part) in the scene.

The colored portion in the image is the detected DCC pixels, whereas the blue

portion is the non DCC portion. The red portion in the center of the cloud represents the

core of cloud whereas the yellowish surrounding portion is the anvil of the cloud. The

uniform single colored patch represents the DCC pixels with similar reflectance. This can

also be seen in the normalized Probability density function of the same scene in Figure

16.
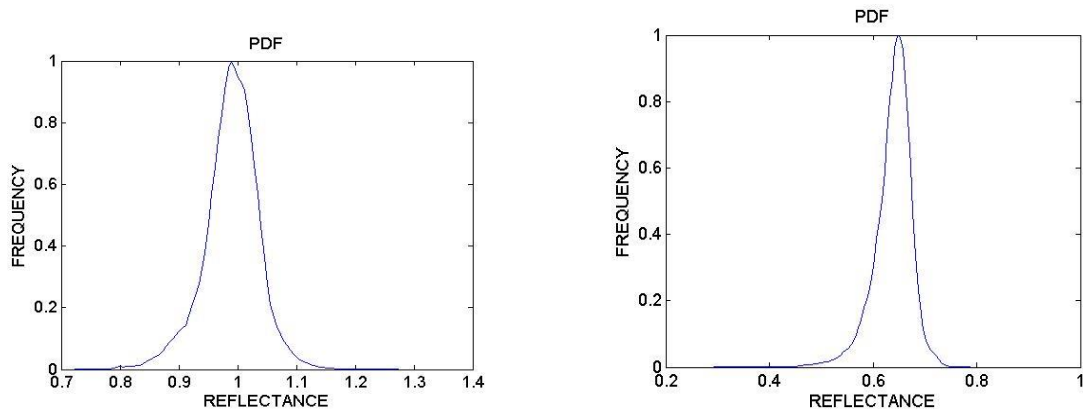
Figure 16: PDF for the DCC pixels for above scene band4 (left) band9 (right).

The probability density function of DCC pixels in each scene shows almost

normal distribution (Figure 16). Although some scenes have PDF with a wide base and

some are skewed. Scenes that have near normal distribution (PDF analyzed with visual

inspection) are passed for further analysis. The single peaked PDF after processing steps

for the scene represents a DCC cloud with uniform reflectance.

3.1.6   SCIAMACHY DCC Spectra and Landsat 8 RSR

To transfer the calibration coefficient from well-calibrated reflected bands to the

cirrus band and coastal aerosol band in Landsat 8, hyperspectral data is required. The

hyperspectral data serves as a transfer medium. With the help of hyperspectral data and

relative spectral response of target sensor, the reflectance or radiance values for different

bands in the target sensor can be derived. Such hyperspectral data for deep convective

clouds were collected by the SCIAMACHY sensor. The DCC hyper spectra shown in

Figure 18 are the average of 46 footprints of Deep Convective Clouds observed by the

SCIAMACHY sensor over the years 2002 to 2012. The flat response of DCC in the entire

range of wavelength can be seen. This flat response of DCC can be used to transfer

calibration from band to bands. This hyperspectral data was provided by Dr. Doelling and

his research team at Langley Research Center, National Aeronautics and Space

Administration, Hampton, VA. (The data was provided as a result of personal

communication between Dr. Helder from SDSU IP lab and Dr. Doelling).
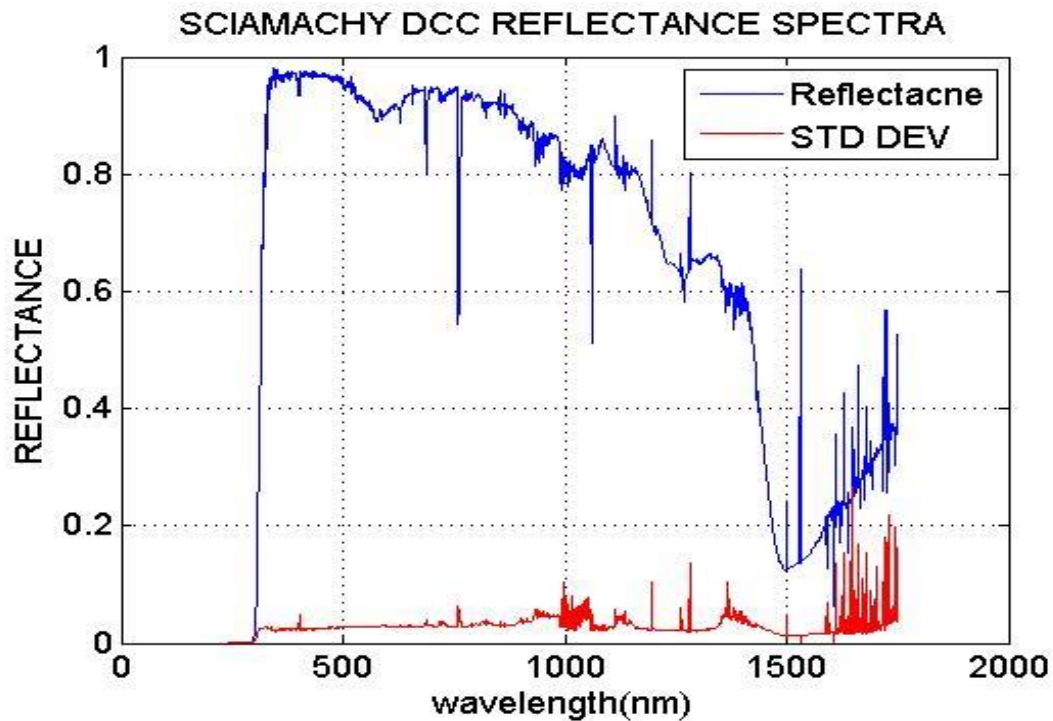
Figure 17: SCIAMACHY DCC spectra (blue) and associated standard deviation (red).

The blue plot is the DCC reflectance for various wavelengths and the red plot is the standard deviation associated with the reflectance calculation for various wavelengths.

The processing of DCC spectra was done by Dr. Doelling and his team. They obtained DCC spectra from SCIAMACHY channels 3 through 6, and it involved the wavelength range from 394 nm to 1750 nm. Channel 3 (394 nm-620 nm) has a spectral resolution of 0.44 nm, channel 4 (604 nm-805 nm) has spectral resolution of 0.48nm, channel 5 (785 nm-1050 nm) have a spectral resolution of 0.54 nm and channel 6 (1000nm-1750nm) has resolution of 1.48 nm [36]. The combined channel 3-6 spectra were obtained using complete, 30x240 km field of view (FOV) observed over a 1 second dwell time. To properly identify DCC within the SCIAMACHY FOV nearly simultaneous collections of cloud properties from Terra MODIS Clouds and the Earth Radiant Energy System (CERES) level 2 single Scanner Footprint (SSF) Edition 2 products were utilized by his team. The Terra spacecraft observes the same region which ENVISAT observes after 30 minutes [37] [28]. Initially MODIS cloud properties were convolved within the CERES 20 Km nominal footprint on the SSF product. From four corners and from the center of the SCIAMACHY FOV, cloud properties were extracted. For all the tropical SCIAMACHY FOVs within $\pm30^{o}$ latitude and 45° SZA to be classified as DCC, the center of SCIAMACHY FOV must have a cloud fraction greater than 99% , cloud temperature should be less than 205K, the cloud optical depth should be greater than 70 and four corners must also have a cloud top temperature less than 205K.

Using the above mentioned procedure 591 DCC SCIAMACHY FOV were identified between August 2002 and December 2010 by Dr. Doelling and his team. Their

investigation revealed that there was inconsistency in channel spectra, especially in channel 5 due to long dwell time. To remove such inconsistency, DCC SCIAMACHY FOVs were further filtered out and 46 FOV were selected that have very similar channel spectra. The standard deviation of the 46 FOV is less than 0.03 for most wavelengths. Thus this DCC spectral dataset contains the brightest equatorial high cloud FOVs found in the earth by SCIAMACHY.

3.1.7   Landsat 8 Relative Spectral Response (RSR)

A sensor records the upwelling target radiance after traversing through the intervening atmosphere. The atmosphere is generally characterized by spectral transmittance (t) and spectral path radiance (Lp). The radiance arriving at the sensor is transferred by sensor optics to the detector focal plane where the image is formed. At this point, multispectral filters, wavelength dispersion devices such as prisms, or a grafting device are used to separate the energy into different wavelengths. The optical path is split into multiple paths, each path with different spectral band filter. The transfer function for each sensor for each band is called the spectral response function (SRF) of the band [18]. Sensor models characterize the process of converting the spectral response of the land-atmosphere system into digital numbers and SRF is one of the most important components of sensor modeling [38]. The SRF is generally presented as the response of a sensor as a function of wavelength and it is also called relative spectral response (RSR) of the sensor. RSR is the curve showing the normalized response of a sensor to light at different wavelengths and is characterized for each spectral band before launch. RSR gives the combined system efficiency including filter transmission and optical sensitivity [18].

Landsat 8 band average spectral responses are shown in Figure 19 along with DCC

reflectance spectra from SCIAMACHY. The Landsat 8 spectral response shown here is

the average response of the 14 FPAs that were measured in each band [**39**] [**9**].
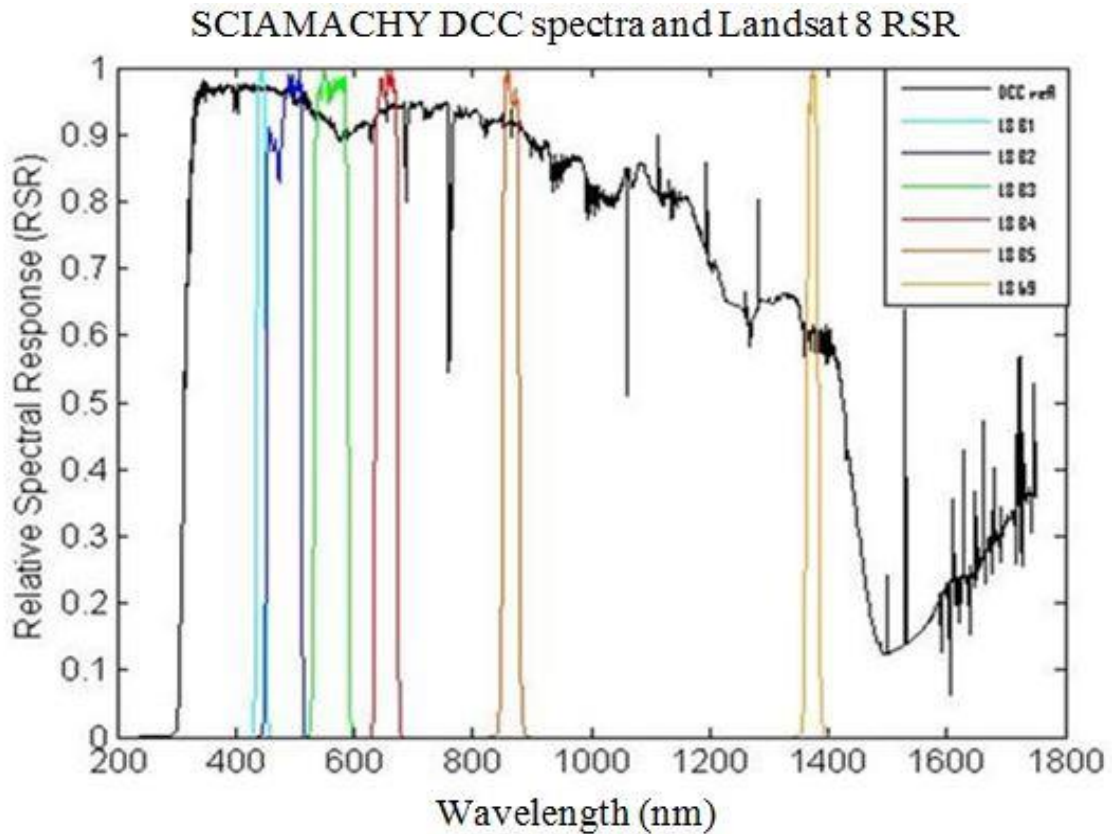
Figure 18: SCIAMACHY DCC spectra and Landsat 8 RSR for various bands [9] [39] **(Date: 09/19/2014).**

3.1.8   Deriving Landsat 8 DCC Reflectance

The SCIAMACHY DCC spectra were convolved with Landsat 8 RSRs and thus

Landsat 8 DCC reflectance was derived for various bands [**9**] [**39**]. Landsat 8 RSR for

band 1 through band 9 and DCC spectra are shown in Figure 18.

The Landsat 8 DCC reflectance is derived by banding the SCIAMACHY DCC spectra with Landsat 8 RSR using the following equation:

$$\rho_{sensor} = \frac{\int \rho_\lambda RSR_\lambda d_\lambda}{\int RSR_\lambda d_\lambda}$$

Where,

ρ_{sensor} = calculated DCC reflectance

ρ_λ = SCIAMACHY derived DCC reflectance

RSR_λ = relative spectral response of each bands

Using the above equation Landsat 8 DCC reflectance for band 1 through band 5 and band 9 are derived. These derived values are tabulated in the table below.

Table 3: Landsat 8 DCC reflectance for various bands derived from SCIAMACHY DCC spectra (Date: 09/16/2014).

Coastal Aerosol	Blue	Green	Red	NIR	Cirrus	SWIR1
0.9688	0.9611	0.9134	0.9371	0.9162	0.5906	0.2228

3.1.9   Scaling Factor (k_i) for Derived Reflectance

The observed mean DCC reflectance was found to be varying up to 10% scene to scene. Since DCC scenes were selected from between 30° N and 30° S, with sun elevation angle less than 30°, the difference in sun elevation angle between DCC scenes affects the reflectance. Similarly there is BRDF effect in DCCs as well [27] [40]. These different phenomena were found have no wavelength dependency but they cause variation in the signal bouncing off the DCC cloud. These variations have to be corrected on a scene by

scene basis. To do this task, the DCC spectra were scaled by scaling factor (k_i) for each

DCC scene. For each DCC scene this scaling factor was obtained by performing the least

square fit between derived L8 DCC reflectance and observed L8 reflectance. In this

process Landsat 8 band 2, band 3, band 4 and band 5 were used. The scaling factor for

which there was minimum root mean square error (RMSE) between observed and derived

L8 DCC reflectance was obtained by using the following equation:

$$RMSEi = sqrt(\sum (OL8j - Ki * DL8j))$$

Where,

K_i = scaling factor (for each DCC scene)

$RMSE_i$ = Root Mean Square Error (for each DCC scene)

$OL8_j$ = observed Landsat 8 DCC reflectance (band 2, band 3, band 4, band 5)

$DL8_j$ = derived L8 reflectance (band 2, band 3, band 4, band 5)

3.2   Results and Analysis

The reflective bands in Landsat 8 (Band 2, 3, 4, 5) are very stable ($< 1\%$) [**41**].

Thus transferring calibration from well calibrated bands to band 9 and band 1 using

DCCs is one of the major goals of this research.

3.2.1   Residual Error Plot

Initially a scaling factor for which there was minimum root mean square error

between observed and derived L8 DCC reflectance was obtained by multiple iterations.

The minimum value of root mean square error was the residue obtained after scaling. For

each scene a unique scaling factor and corresponding residue (RMSE) is obtained. Figure 19 shows the plot between mean reflectance and residue for each DCC scene that was analyzed.
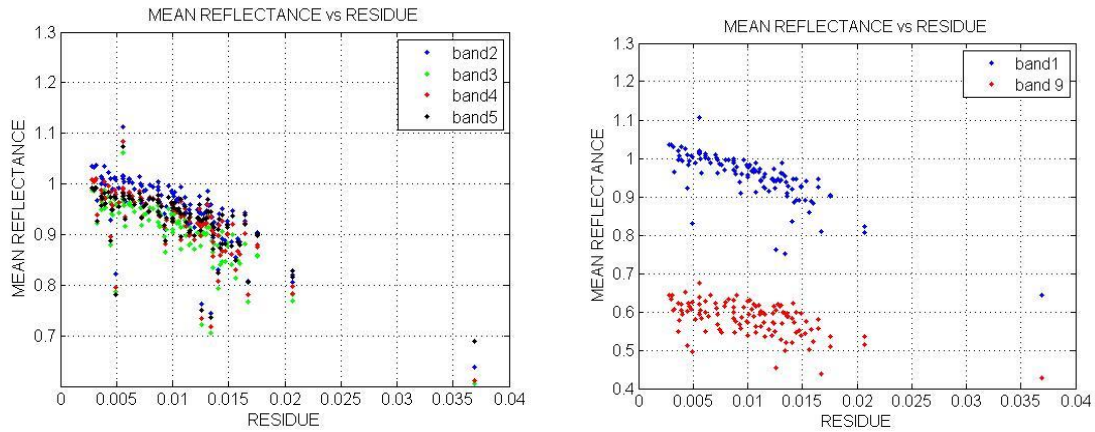
Figure 19: Plots showing mean reflectance of each DCC scenes and residue obtained during calibration. (Left) bands used in inter-band calibration, (right) bands whose calibration coefficient was obtained.

The Y axis of the plot shows the mean reflectance of each DCC scenes and the X axis show the residue (RMSE) during inter-band calibration. The left plot shows mean reflectance of band 2, 3, 4, 5 for all the DCC scenes and the residue in the inter band calibration. The right plot (Figure 19) shows the observed reflectance of band 1 and band 9 and the residue obtained during calibration. Less variation was observed in the reflectance plot of band 1, whereas for band 9 there was more spread in the plot. Carefully analyzing the residue and scene mean reflectance, it was observed that there was a large variation in scene mean when residue is greater than 0.012. Higher residue indicates that the spectra are not fitted properly to the observed data. To remove those ill-fitted scenes, scenes having residue greater than 0.012 were removed, and scenes having residue less than 0.012 are passed on for further analysis.

3.2.2　Scaling Factor vs. Reflectance Plots
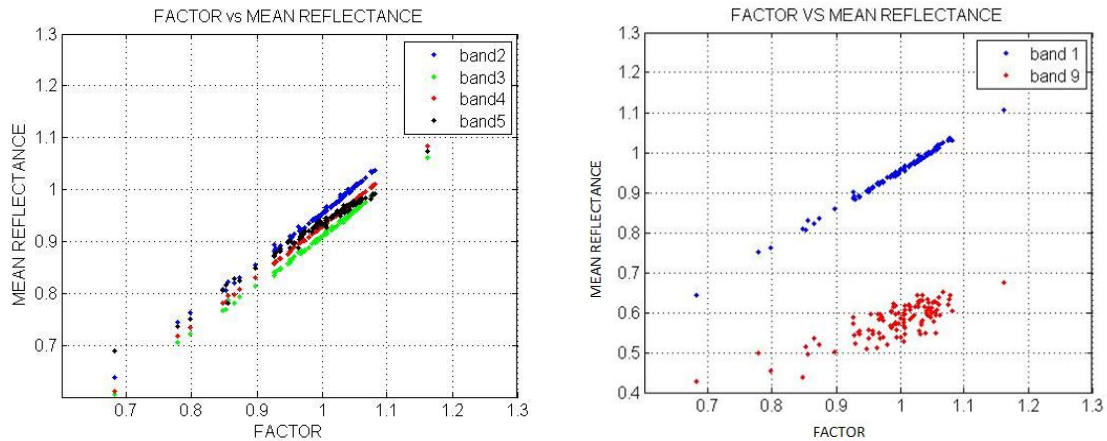
Figure 20: Scaling factor vs. scene mean reflectance for band 2- 5 (left). Scaling factor vs. scene mean reflectance for band 1 and band 9 (right).

The factor scales derived Landsat 8 reflectance for each band to remove variation of DCC reflectance scene by scene. Mean reflectance (band 2, 3, 3, 5) of each DCC scene and their corresponding scaling factor are plotted in Figure 20 (left). The individual plots for each band used in calibration can be seen in Figure 21. The mean DCC reflectance for these bands can be seen as linearly increasing with increasing scaling factor (Figure 20 (left)). This result was expected because for a scene showing relatively higher mean reflectance, the spectra should be scaled by higher value and that with low DCC scene mean should be scaled by a lower scaling factor. The clouds that are extending really up in the tropopause layer would reflect most of the signals and thus show high reflectance whereas clouds having somewhat low height will exhibit lower reflectance. Band 5 is showing some deviation from linear increment with scaling factor. Similarly scene mean DCC reflectance of cirrus and coastal aerosol band and scaling factor are plotted in Figure 20 (right). The increasing scene mean trend of the coastal aerosol band and cirrus band with the increasing factor can be seen in Figure 20 (right). Scene-by-scene more

variation can be seen in cirrus band reflectance as compared to reflective bands. This can be seen in figure 20.
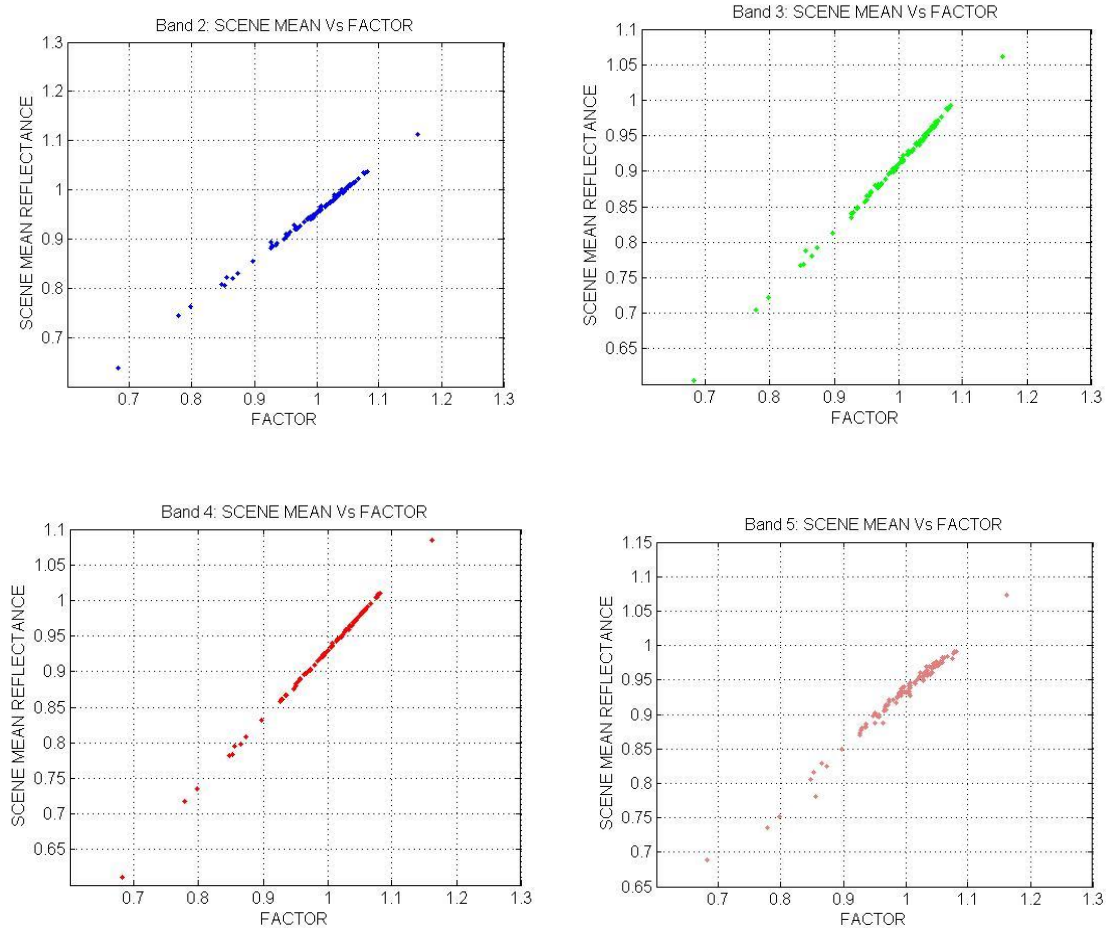
Figure 21: Scaling factor vs. scene mean reflectance for each band used in inter-calibration. All bands are showing linearly increasing with factor, except band 5 which is slightly deviating (Top left: band 2, top right band 3, bottom left band 4, bottom right band 5).

Scenes having a higher scaling factor were found to have higher scene mean reflectance and vice versa. Since DCC are bright targets, the less bright scenes might not be DCC scenes. Also from Figure 20 (left), most of the scenes have a scaling factor of less than 0.9 and have slightly more variation in scene mean reflectance. Thus to avoid such possible non-DCC scenes, the scenes having a scaling factor less than 0.9 are avoided for further analysis

3.2.3   Gain Estimation and Analysis

All the scenes having residue error (in band-to-band calibration) greater than

0.012 and scene having scaling factors less than 0.9 were removed from further analysis.

Using the remaining 72 DCC scenes further analysis was done. For each DCC scene, the

derived DCC reflectance for band 1 and band 9 was scaled by its corresponding scaling

factor (K_i) and the gain was determined using the following relation.

$$Gain(G) = \frac{Landsat\ 8\ observed\ DCC\ reflectance\ for\ Band\ A}{scaling\ factor(ki) * derived\ DCC\ reflectance\ for\ Band\ A}$$

The gain determined using this process is shown in the plots below.
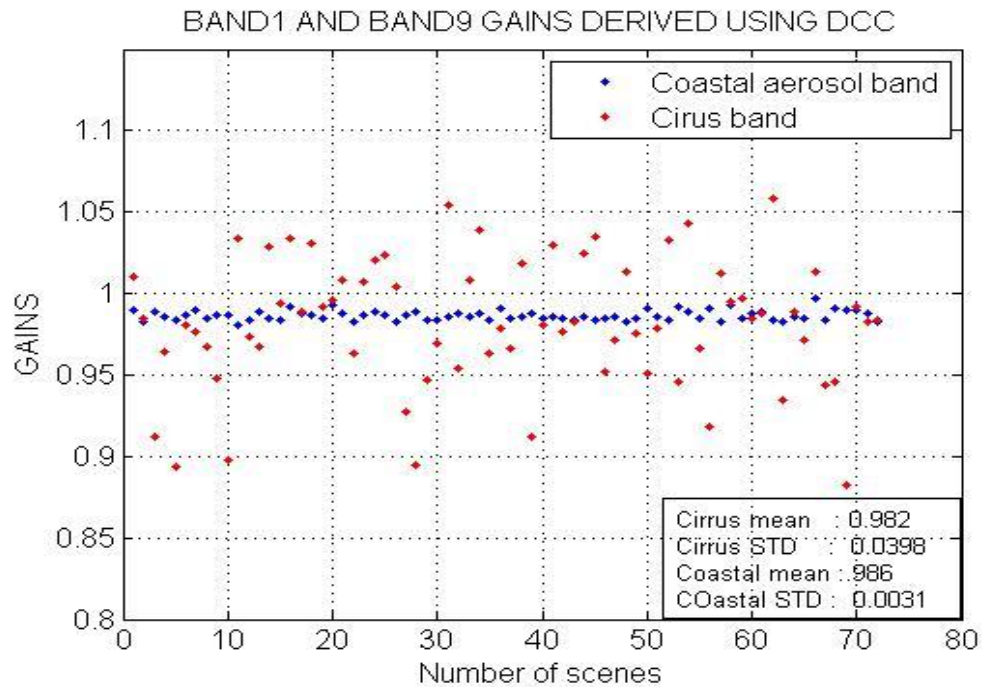
Figure 22: Gain plots of band 1 and band 9 obtained using 72 DCC scenes.

Band-to-band calibration showed that the gain of the coastal aerosol band is

around 1.5% off with respect to reflective bands (bands 2, 3, 4, 5). The gain estimate for

cirrus band was 0.982 ±0.0398.Similarly the gain estimate for coastal aerosol band was

0.986 ± 003. These results can be considered as very good results as the precision level in

gain estimate for both the bands is above 96%. The precision level for coastal aerosol

band is higher in comparison to cirrus band. Figure 22 shows estimated gain for band 9

(red dots) and band 1 (blue dots). The gain estimates were analyzed with respect to

different parameters such as residues in the procedure and scaling factor.
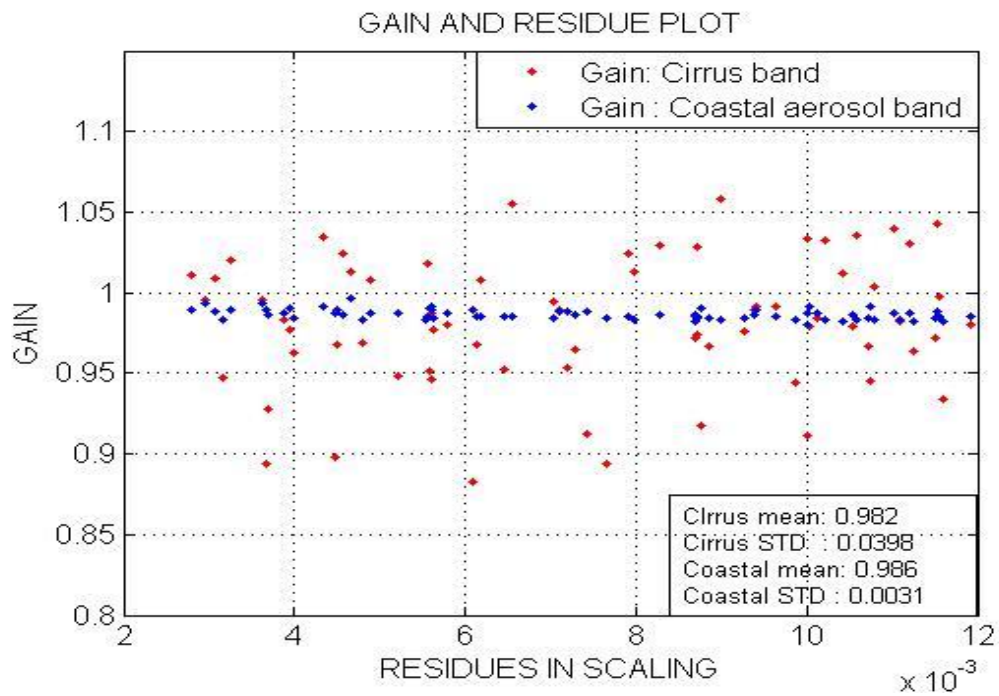
Figure 23: Gain and residue plot.

Figure 23 shows variation of gain with the residue obtained in scaling the spectra.

Gain estimate for cirrus band shows larger variation but the obtained results are well

under the set goals of 5%. These results exhibit the robustness and high precision of this

calibration technique.

There is very small dependency of gains with residue. With increase in residue, slight decrease in gain value was observed, but for residue less than 0.012 this change is very small and is neglected. Figure 24 is the plot of obtained gains and scaling factor.
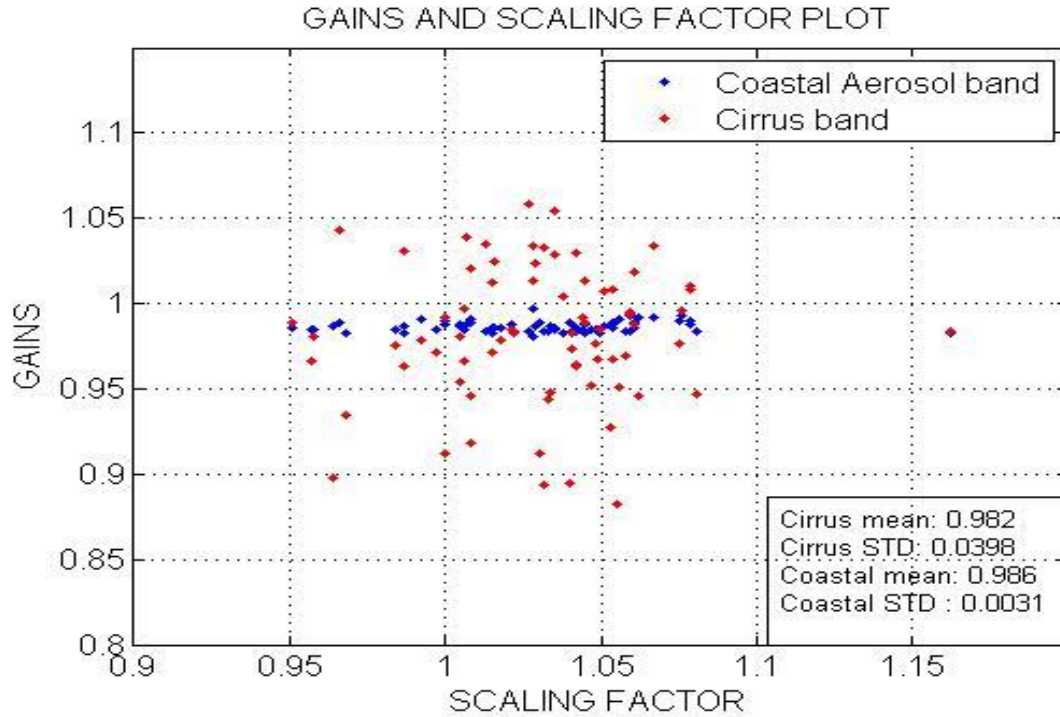
Figure 24: Gains and scaling factor plot.

By observing the plot between gains and scaling factor, it can be seen that there is no dependency of gains with scaling factor.

3.2.4   Possible Explanation for Variation in Estimated Gain of Cirrus Band

The results on the coastal aerosol band have higher precision than that of cirrus band. The variation in the gain estimate of cirrus band might have been caused by various factors, such as effect due to cloud height. During this research, effect due to cloud heights was not taken into account. DCC clouds can have different heights. The DCC clouds at comparatively low height still might be lower in atmosphere such that there is a

small amount of water vapor absorption between the cloud top and the sensor. This small amount of water vapor in the high atmosphere might have absorbed the signal causing variation in the signal reflecting from the cloud tops. The cirrus band operates in the water vapor absorption band whereas the coastal aerosol band is away from atmospheric water vapor absorption; hence the cirrus band is affected by such water vapor present in the higher atmosphere above the cloud tops. Thus, detection of these lower height clouds as DCCs might have caused the variation in cirrus band gain estimate.

To better understand the variation in gain estimate of cirrus band a MODTRAN simulation was run in the SDSU image processing lab by Imaging Engineer Larry Leigh. The simulation was performed for a range of wavelength with various parameters of DCC such as brightness-temperature, geometric parameters and heights of clouds. In this simulation the DCC reflectance for various wavelengths and various cloud heights was observed. The obtained results can be seen in Figure 25.
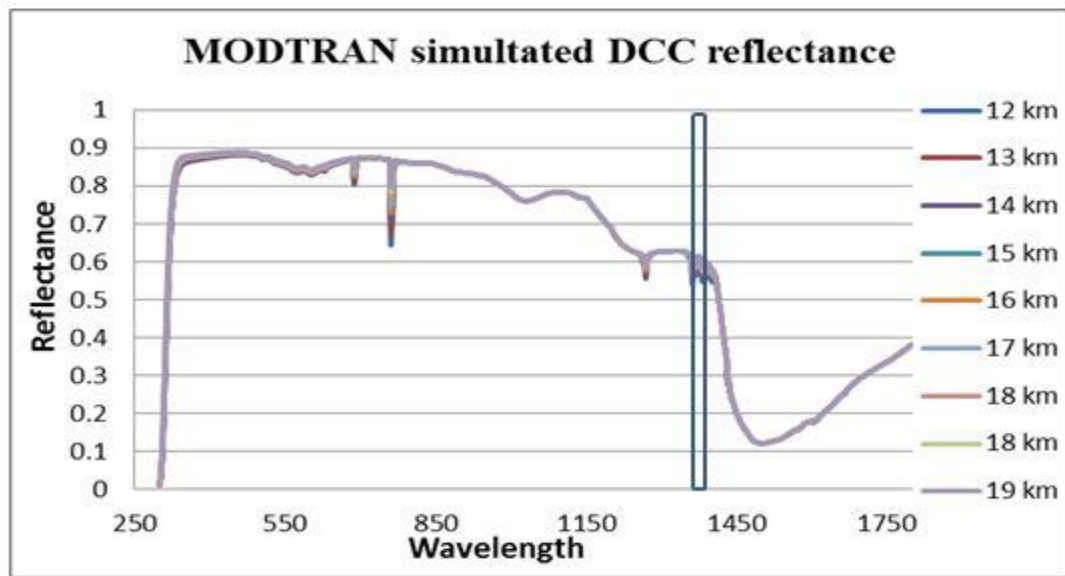
Figure 25: The MODTRAN simulated DCC reflectance spectra at different cloud heights.

Figure 25 is the MODTRAN simulated DCC spectra. The blue horizontal bars in the plot show the operating wavelength of cirrus band. The simulated DCC spectra are spectacularly similar to DCC spectra from SCIAMACHY. The simulation was done for cloud heights from 12 km to 19 km. To further analyze, the reflectance plot for the range of cirrus band was observed as shown in Figure 26. Figure 26 shows that there is variation in DCC reflectance due to cloud height in the range of wavelength where cirrus band operates.
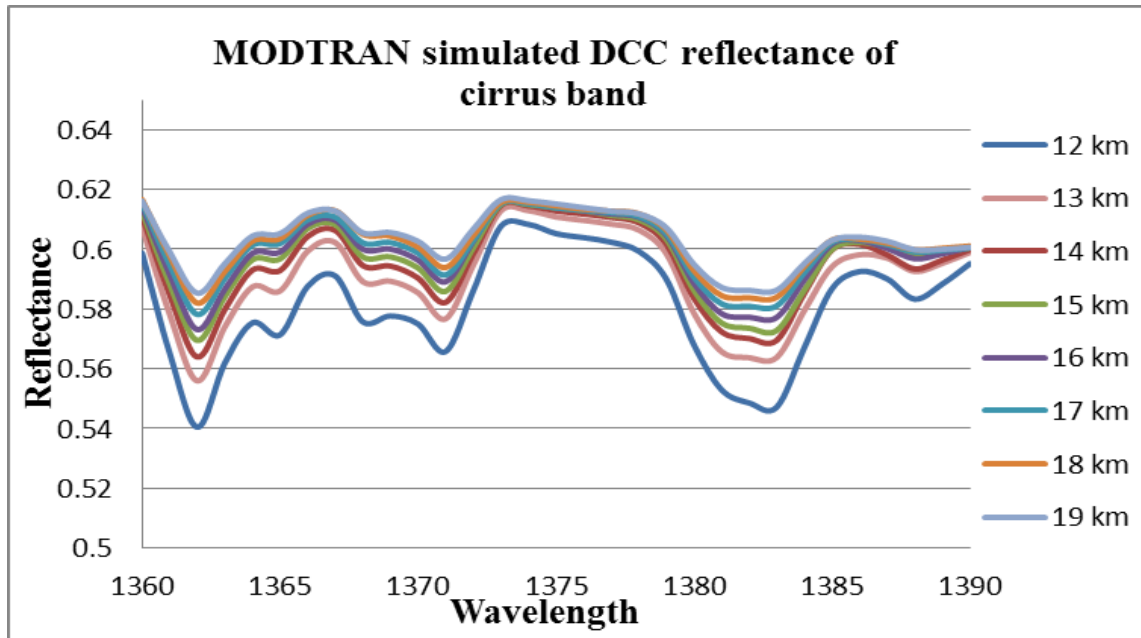
Figure 26: Simulated DCC spectra in the range of cirrus bandwidth.

The cirrus band is centered at 1375nm, and it has lower band edge of 1360 and upper band edge of 1390 nm. To quantify the results, the reflectance data were banded up for all the bands. The banded results are shown in table 4. The change in DCC cloud height from 12 Km to 19 Km affects the reflectance of the coastal aerosol band by 0.0081 reflectance units, whereas its affects cirrus band by 0.0224 reflectance units.

Table 4: Mean reflectance from simulated cloud heights.

	CA	Blue	Green	Red	NIR	Cirrus	SWIR1	SWIR2
12 km	0.8814	0.879	0.8457	0.8598	0.8511	0.5826	0.1913	0.2413
13 km	0.883	0.8803	0.8471	0.8607	0.8512	0.5924	0.1915	0.2418
14 km	0.8844	0.8815	0.8488	0.8616	0.8513	0.5966	0.1917	0.2421
15 km	0.8856	0.8826	0.8505	0.8626	0.8513	0.5988	0.1919	0.2424
16 km	0.8868	0.8836	0.8521	0.8635	0.8514	0.6007	0.192	0.2427
17 km	0.8878	0.8845	0.8537	0.8644	0.8515	0.6022	0.1922	0.2429
18 km	0.8887	0.8854	0.8553	0.8654	0.8515	0.6038	0.1923	0.2431
19 km	0.8895	0.8862	0.8573	0.8665	0.8516	0.605	0.1923	0.2432
Mean	0.8859	0.8829	0.8513	0.8631	0.8514	0.5978	0.1919	0.2424
Max-min	0.0081	0.0072	0.0116	0.0067	0.0005	0.0224	0.001	0.0019

The variation in reflectance due to cloud height was observed to be very small for reflective bands and the coastal aerosol band (0.55%). For the cirrus band, this effect was around 4%. Thus from this simulation it was evident that the change in cloud height can vary the signals reflecting from the DCC clouds in the range of wavelength where cirrus band operates. From this simulation it is evident that, variations in the DCC cloud height were found to be the major source of variability in the gain estimate.

CHAPTER 4

4   RELATIVE GAIN ANALYSIS OF CIRRUS BAND USING DCC SCENES

As explained earlier, ideally every detector made from the same materials at the same time should respond similarly when the same input is applied. However, practically, detectors from the same array show different responses even though the same input is applied to each detector. This unequal response of detectors degrades the quality of the image. In order to retain the quality of image data, correction factors need to be applied. Generally, these correction factors are estimated based on the technique of histogram equalization. Relative calibration based on scene statistics uses the histogram equalization method. In this method, relative gain is estimated from first and second order statistics obtained from image data. The gains can be calculated with respect to an individual reference detector or the average of all operative detectors. This method works for whiskbroom type of sensor but for push-broom sensors, such as Landsat 8, such a method doesn't work because a detector at one end of an array does not measure an identical radiance level as the detector at the other end of the array. Thus, a statistical approach can be applied for push broom sensors where relative gain is estimated by averaging the composite detector statistics obtained from a large number of images [**23**].

4.1   Cirrus Band Configuration in Focal Plane

The cirrus band is one of the nine operating bands in Landsat 8. The optical system of OLI collects radiant energy from targets on earth. This radiant flux enters the aperture of OLI and projects onto the focal plane. The incident energy is filtered such that different wavelengths (generally described in terms of bands) of energy are passed to

different focal plane elements. Thus detectors in each band on OLI are irradiated by light with corresponding wavelength. (E.g. detectors in red band get hit by light having wavelength around 655nm).

As previously mentioned OLI focal plane is comprised of 14 Focal Plane Modules (FPMs). Each FPM contains an array of detectors for every band. The 14 SCAs are arranged in staggered fashion [13]. Figure 27 shows the configuration of different bands in the focal plane.
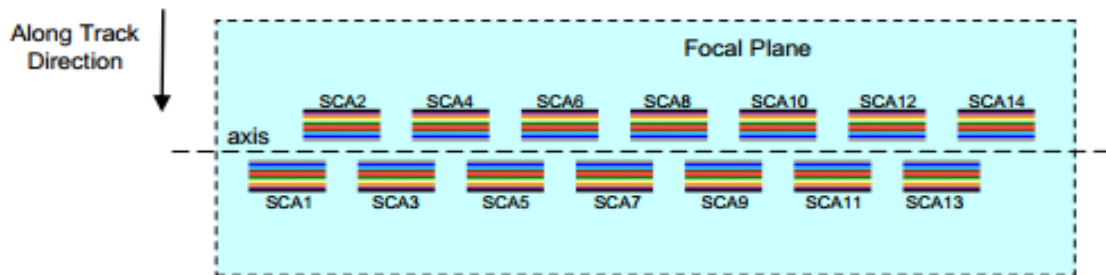

Figure 27: FPM placement in focal plane of OLI [13]**.**

It can be seen in Figure 27 that two rows of FPMs are arranged on either side of the horizontal axis. The different color in each FPM represents different bands. Figure 28 shows the detailed organization of bands in each FPA and its adjacent FPA.
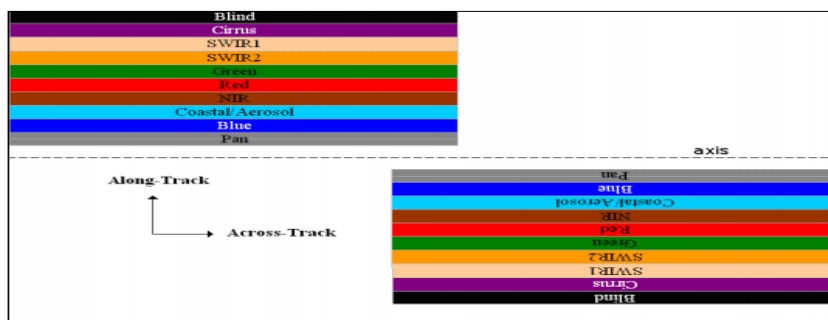
Figure 28: Detector placement on adjacent FPMs [13]**.**

The adjacent FPMs are rotated 180 degrees with respect to each other. In each FPM, the cirrus band lies at the far end from the focal plane axis.

4.2 DCC Scenes and Per-detector Response

The clouds are in random shapes, and are moving randomly, therefore, a single DCC cloud, filling an entire FOV of Landsat 8 is difficult to capture. Thus a statistical approach was analyzed. The detector responses from a large number of DCC scenes were averaged. In OLI there are 14 FPMs and each FPM has 494 detectors for each band. Thus the average response of 494 detectors was obtained by binning these DCC scenes and then was used to estimate the relative gain of the cirrus band.

DCC scenes used in this process were identified using the same process as described in Section 3.2.1. To identify scenes with a large number of DCC pixels and to avoid scenes with few DCC pixels stricter thresholds than described in section 3.2.1 were used. All the scenes between $+30^o$ latitude, and -30°, latitude, having the sun zenith angle less than 30°, having the scene mean brightness temperature less than 220K in band 10 (10.8 micron), the scene mean radiance in band 4 (665 micron) greater than 220 watts m^{-2} sr^{-1}, and having the scene mean radiance greater than 30 watts m^{-2} sr^{-1} in band 9 (1375nm) were identified as DCC scenes. All together 69 DCC scenes were obtained from the method.

Per-detector response for each selected scene for band 9 was obtained from the image Assessment System (IAS). The per-detector response is the average response of each detector on the band when it views a single scene. It can also be considered as a pixel column average. It represents the average value of the observed radiance (in terms

of DN value) by a single detector in a single frame. The concept can be explained in the simple Figure 29 below.
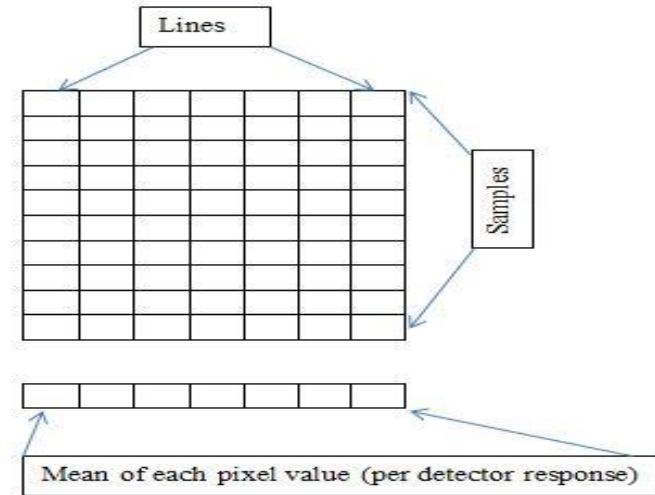
Figure 29: Conceptual image showing pixels and per detector response.

The conceptual image in Figure 29 represents a satellite image. An image consists of rows and columns of pixels. The rows are also known as samples whereas columns are known as lines. The per-detector response is the average of each column of pixels throughout the image.

The detector response for each scene is averaged and finally average per FPM response is obtained for each FPM. The main assumption is that for enough number of DCC scenes, the averaged response of all the detectors will be same. This average response was applied to obtain the relative gain for each detector in the FPM for band 9. The obtained gain values for each detector were applied to different test scenes to validate the results.

4.3   Relative Gain

The relative gain for each detector was obtained using average per detector response obtained by binning 69 DCC scenes. The gain was estimated on a per FPM basis. A simple relation below explains the relative gain for each detector.

$$Rel\ Gain\ per\ detector = \frac{Average\ response\ of\ a\ detector\ on\ a\ FPM}{Average\ response\ of\ that\ FPM}$$

The gain for each detector obtained from DCC method is shown in Figure 30. The relative gains on either ends of FPM show different shape as in Figure 30. This indicates that the relative gain of the detector is the function of its position in FPM.
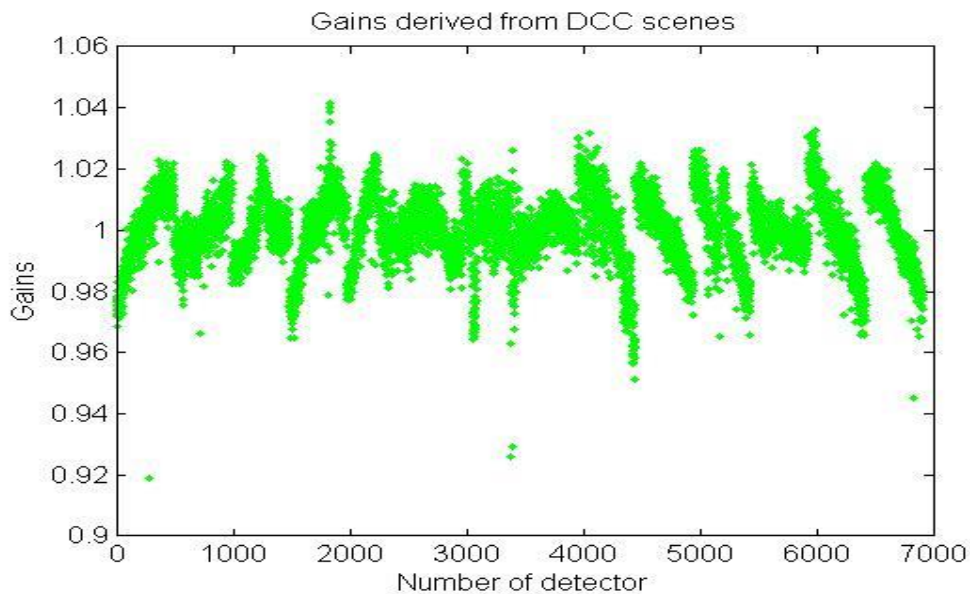
Figure 30: Plot showing the gain derived from composite DCC scenes.

The FPM on the left side of the array has increasing gains but the FPM on the right side of focal plane has decreasing gains, whereas the central four FPM don't have considerable gain change.

Considerable discontinuities at the FPM boundaries can be seen in the gain plot in figure 30. These discontinuities are seen because gains were calculated on a per FPM basis. In this process the normalization of FPM boundaries was not performed.

4.4   Applying Relative Gains to the Test Scenes

Two types of test scenes were used to test the obtained gains. First, test scenes were selected from the same scene list as those that were used for deriving the gains. Gains were applied to bias removed (L1Rp) images and the result shows that the image quality was improved. Visible streaking in the image was removed and the image shows good quality. The results were verified visually as well as quantitatively using the streaking metric. The streaking metric was considerably decreased after applying DCC derived gains. In almost all the scenes streaking was below 0.2 after the gain was applied. The results accomplished the goal of obtaining streaking below 0.2.

The other set of scenes was taken from the scenes where scenes were not used to derive the gains. Gains were applied to bias removed (L1Rp) images and the results showed that the image quality was drastically improved. All the visible streaks were removed and the images show good quality. The results were also verified using the streaking metric. The streaking metric was considerably decreased after applying DCC derived gains. For all the scenes, the streaking metric was below 0.2 after the gain was applied. The results were compared to results obtained by applying gains from default CPF. The streaking metric for the scene when DCC gains were applied was considerably lower than that of scenes where the CPF gain was applied.

4.5   Qualitative Analysis

For visual analysis, L1Rp, FPM level scenes were obtained from the IAS. These

scenes are bias removed and gain was not applied. After deriving gains from DCC

scenes, they were applied to each of them. The visible streaks were removed after gain

was applied. The image quality was improved drastically. The results were also compared

with the same image when default CPF gains were applied to the image (Scene id:

LC80720142013222LGN00).
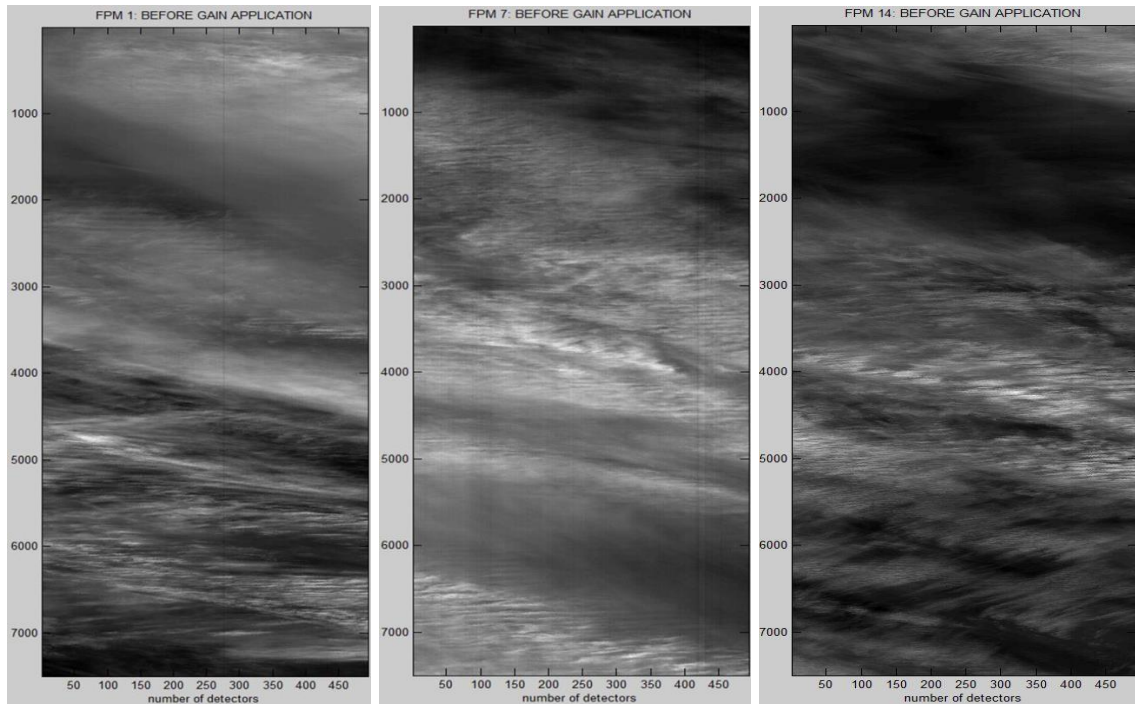
Figure 31: FPM 1 (left) FPM 7 (middle) and FPM 14 (right) before gain applied. Visible streaks are easily seen in these L1Rp scenes.
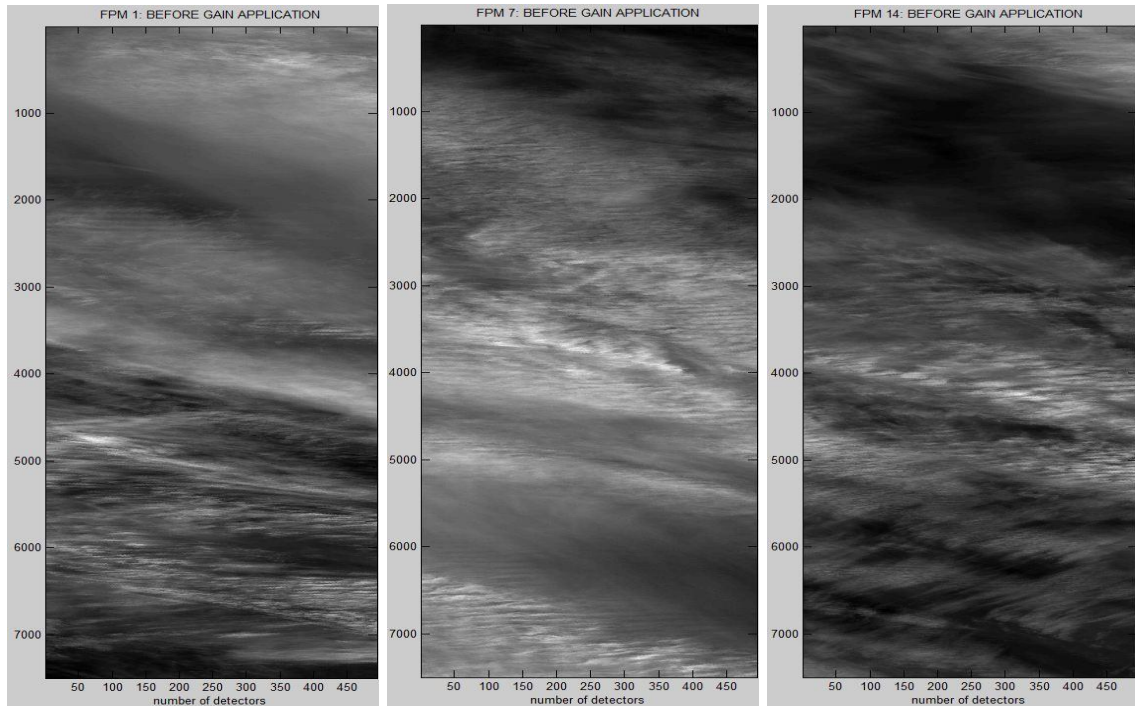
Figure 32 FPM 1 (left) FPM 7 (middle) and FPM 14 (right) after DCC gain was applied. Streaks are no longer visible after new gains were applied.

In each set of scenes, three images can be seen. These images are from FPM 1, FPM 7 and FPM 14 respectively of a single L8 scene. A Landsat 8 scene consists of 14 FPM so 14 different such scenes are observed for each scene. But for ease in representation, only three FPMs images per scene are shown. Before the application of any gains to the scenes, there are many visible streaks all over the scenes (Figure 31). But after the DCC derived gain was applied to the scene, the visible streaks were removed. Thus the image quality is improved (Figure 32).

A qualitative comparison was also performed using a L1T scene when default CPF gain and DCC gain were applied.
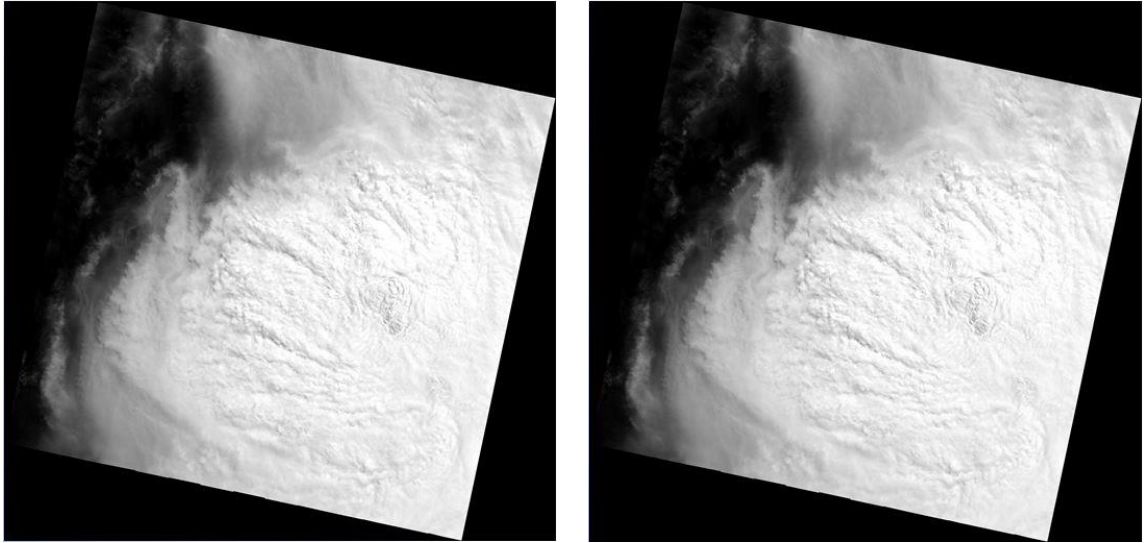
Figure 33: L1T image after DCC derived gains were applied (left) and when default CPF gain were applied (right).

This image in Figure 33 (scene id LC80120552013170LGN00) shows a L1T

scene when processed using DCC derived gains and default CPF gains respectively. After

applying DCC gain the image quality was increased and the L1T scene was of good

quality. But details in the scenes were not visible, so it was hard stretched as shown in

Figure 34 and figure 35.
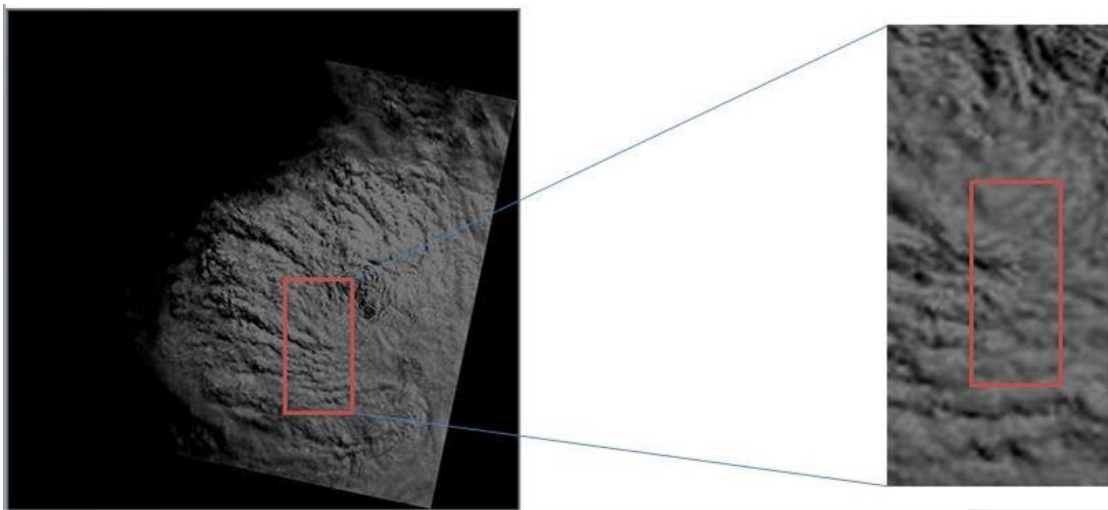
Figure 34: Hard stretched image after CPF gain were applied.
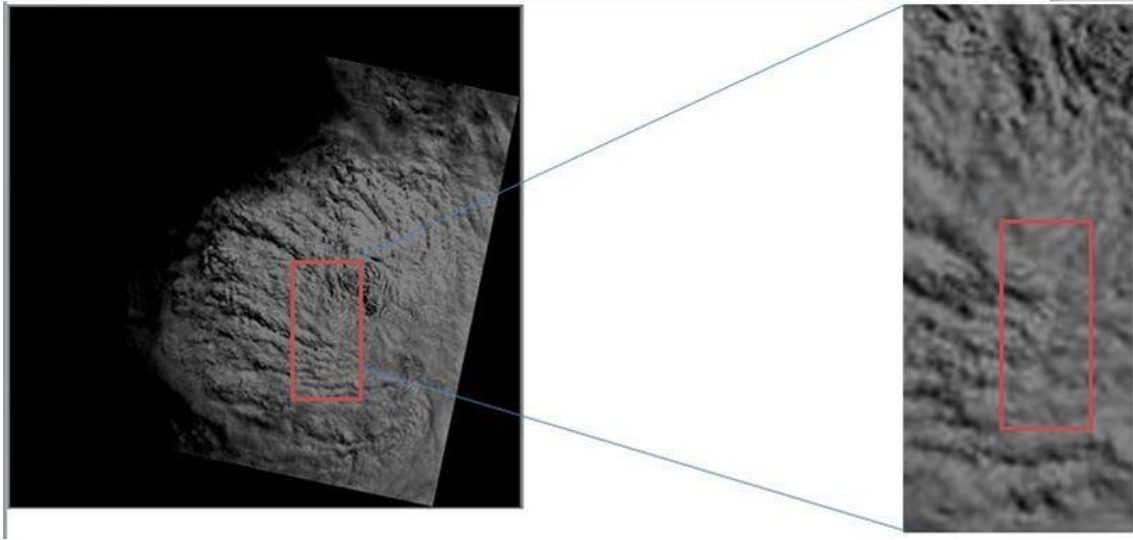
Figure 35: Hard stretched image after DCC gains were applied.

Figure 34 and 35 are the stretched image of the same above image in Figure 33. After stretching the image, FPM boundaries are slightly visible when closely examined. These boundaries are seen because the FPM boundary normalization was not applied to the scene while processing.

4.6   Quantitative Analysis Using Streaking Metric

The results were also analyzed quantitatively using a streaking metric. A streaking metric indicates the amount of streaks present in the image. The lower the value of the streaking metric, the lower is the number of streaks present in the image. The streaking metric gives a simple quantitative measure of variability in response between adjacent detectors. It gives the normalized difference in mean DN count of the ith detectors with the average of $i-1^{th}$ and $i+1^{th}$ detector. The streaking metric can be represented by following simple relationship.

$$S_i = \frac{\left| \bar{L}_i - \frac{1}{2}(\bar{L}_{i-1} + \bar{L}_{i+1}) \right|}{\bar{L}_i} \quad [\mathbf{12}]$$

Where,

S_i is the streaking metric for the ith detector

$\bar{L}_i$ is the mean DN count for the detector

The quality of image when DCC gain was applied and when CPF gain was applied were compared using the streaking metric. For most of the detector in the entire focal plane array, the streaking metric was below 0.2. The streaking metric also shows that DCC derived gain works better than default CPF gain. These results can be seen in Figure 36 for different scenes. The streaking metric was normalized by the average response of each FPM.
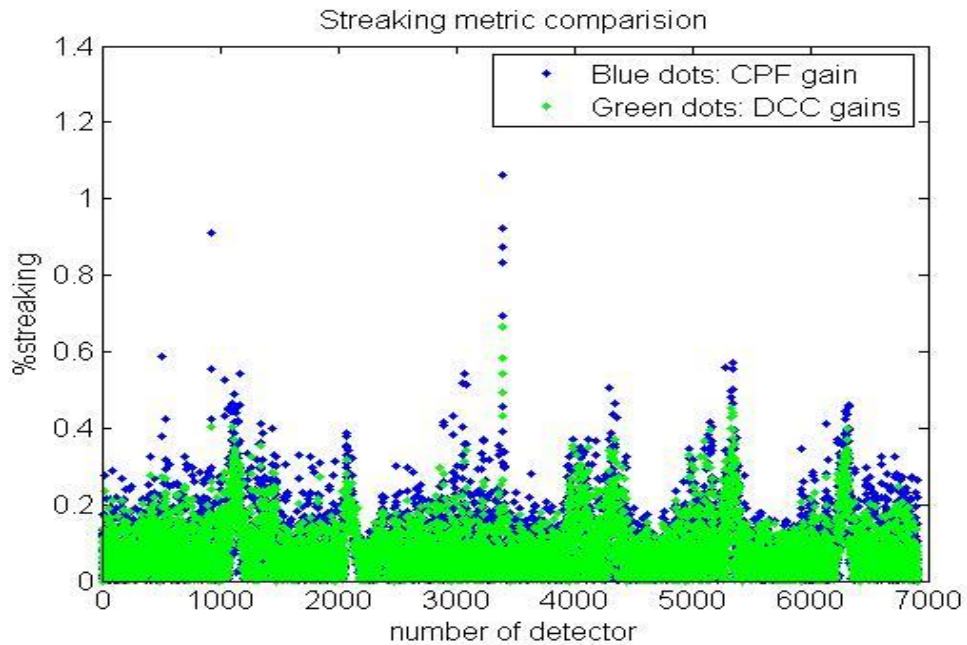
Figure 36: Streaking metric for a scene when DCC derived gains were applied (green dots), when CPF gain was applied (blue dots) (LC80720142013222LGN00).
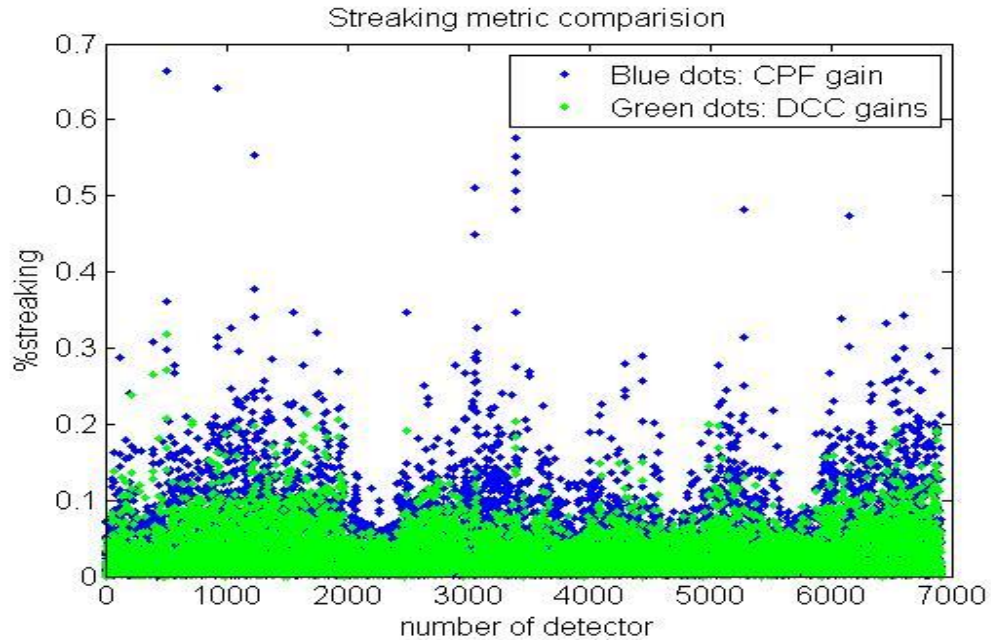
Figure 37: Streaking metric for scene when DCC derived gains were applied (green dots), when CPF gain was applied (blue dots) (LC81990502013184LGN00).

The blue dots represent the streaking for each detector when the default CPF gain was applied and the green dots represent the streaking due to DCC derived gain. The percent streaking for detector was below 0.2 for the most part. It can be seen that, for the most part the DCC derived gain outperforms the CPF gain. The 0.2 streaking metric is less than the required specification for the cirrus band. Thus it is evident that the DCC derived gains are working better than the default gains.

CHAPTER 5

5   ERROR ANALYSIS, DISCUSSIONS AND CONCLUSIONS

In this chapter, the possible sources of errors during the band to band calibration process are presented. The results are discussed and required steps in the future work are discussed.

5.1   Major Sources of Error

The error involved in the entire process of band to band calibration using DCC as inter-band calibration sources is presented in this section. The DCC spectra from SCIAMACHY were taken as a medium to transfer calibration. The band to band pixel misregistration in Landsat 8 was neglected for the entire process. The SCIAMCHY has large GSD of 30x250km, whereas Landsat 8 has small spatial resolution of 30m. The effect due to the difference in spatial resolution of two sensors was not considered in this research. The possible sources of errors can be sorted in two groups.

5.1.1   Error during DCC Detection

There can be errors during the initial process of DCC detection. Initially DCC pixels are detected using an Infrared threshold, thermal and IR spatial homogeneity threshold in each scene. Typically, DCCs are in different stages of their life cycle. Some are imaged as pristine DCC pixels whereas some are anvils of clouds that are as cold as DCC pixels themselves. Thus during DCC detection many false DCC pixels may also be detected. This false detection of DCC can cause an error in the overall analysis.

The main effect of these non-DCC pixels is in the change in the scene's mean DCC reflectance. The reflectance of these non-DCC pixels will not be uniform and does not behave like near Lambertian surface. The DCC reflectance PDF for scenes with a large number of non-DCC pixels will be different than that of those having a large number of good DCC pixels. The mean value of DCC reflectance PDF will be shifted either high or low depending on the amount of false DCC pixels detected. If this shift in the mean is assumed to be the same for all bands under consideration, it can be shown that the error due to this shift is minimal. This shift in mean value might affect the absolute calibration using DCC targets, but for band to band calibration this effect is minimal, if an equal shift in the mean of PDF for all bands is assumed.

In this research, a scaling factor was estimated for each scene. The scaling factor was obtained by minimizing the root mean square error between the observed reflectance value and the derived reflectance value. This scaling of derived reflectance minimizes the error due to the false detection of DCC. This can be shown mathematically in the following equations.

The RMSE error during scaling is given by the equation described in section 3.2.9

$$RMSEi = sqrt(\sum(OL8j - Ki * DL8j)^2)$$

For very small RMSE error, we can write the equation as follows:

$$\sum(OL8j - Ki * DL8j)^2 = 0$$

$$(OL8j - Ki * DL8j) = 0$$

$$(OL8j = Ki * DL8j)$$

Considering for a scene and a single band we can write

$$(OL8 = K * DL8)$$

Now the false detection of DCC will affect the left hand side of equation and it will be shifted. Let us denote the shifted scene mean due to false DCC detection as

$$(OL8' = M * OL8)$$

Here OL8' is new scene mean reflectance due to false DCC detection and M is the scaling factor by which the scene mean is shifted due to false DCC detection.

Again an equation can be used to find the RMSE error when there is false detection of DCC and we can obtain a scaling factor. This can be shown below.

$$RMSEi = sqrt(\sum (OL8'j - K'i * DL8j)^2)$$

Here, K' is the scaling factor obtained by scaling the scenes where there are false detection of DCC and OL8' is the observed scene mean of false detected DCC scene, then;

$$(OL8' = K' * DL8)$$

$$M * OL8 = K' * DL8$$

$$M * OL8 = K' * DL8$$

$$OL8 = (K'/M) * DL8$$

From the above equations,

$$K = (K'/M)$$

The final expression from the above analysis shows that the shift in the scene mean due to false detection of DCC is compensated by the scaling factor estimated for the scene with false DCC detection. If the scene mean is shifted to low value due to non DCC pixels, this shift is seen in all the bands used in calibration. Similar shift will be seen in band 9 and band 1 as well. The linear trend in mean reflectance with increasing scaling factor also suggests that such a shift occurs for at least all reflective bands. Further investigation is needed to validate the effect of false DCC detection and its effect in reflectance.

5.1.2   Errors during Calibration

5.1.2.1   Residue during Fitting the Data

After the DCC pixels are detected, reflectance of each DCC pixel was calculated. The scaling factor for each scene is calculated by performing a root mean square fit between observed DCC reflectance and derived DCC reflectance. After scaling the observed DCC reflectance for each band is not exactly equal to the derived DCC reflectance from spectra. This difference can be seen in the residue of the fit. The residue (RMSE) was less than 0.012 units for all the scenes in consideration. For overall error analysis this residual error should be considered in the calculation.

5.1.2.2   Uncertainty in of Landsat 8 Reflectance Calculation

The uncertainty of Landsat 8 for reflectance calculation was less than 1 % for all bands. Four reflective bands were used to transfer calibration to the cirrus and coastal

aerosol bands. This uncertainty in Landsat 8 reflectance is very small, but is also transferred to the estimated gains. Thus this uncertainty in Landsat 8 needs to be considered for the overall uncertainty of band to band calibration.

5.1.2.3   *Uncertainty in SCIAMACHY DCC Spectra*

The calibration accuracy of SCIAMACHY spectra used in the band to band calibration varies within operating wavelengths (channels to channels) [**42**]. The errors in SCIAMACHY reflectance can be summarized in the Table 5 [**42**].

Table 5: Table summarizes the errors in different SCIAMACHY channels.

Channel	Ch 1	Ch 2	Ch 3	Ch 4	Ch 5	Ch 6	Ch 7	Ch 8
Spectral Range (nm)	240 -314	309 - 405	394 - 620	604 - 805	785 - 1050	1000 - 1750	1940 - 2040	2265 - 2380
Errors	3%	4%	3%	2%	6%	4%	3%	3%

The DCC spectra are obtained from channel 3 to channel 6. The hyperspectral DCC spectra are used as transfer medium and are scaled scene by scene in the band to band calibration process. But the different wavelengths of spectra have varying uncertainty, and thus might generate errors in the process. Relatively high uncertainty can be observed in channels 5 and 6. Channel 5 and 6 in SCIAMACHY corresponds to wavelength range of the cirrus band in Landsat 8. So the uncertainty in different channels of SCIAMACHY should be considered in band to band. Table 6 lists the possible sources of errors in the entire process.

Table 6: List of possible sources of errors in band to band calibration process.

		Possible Sources of Errors
	1	**Errors during DCC detection**
	a	False detection of DCC pixels
	b	Possible band to band pixels misregestration
	2	**Errors during band to band calibration**
	a	Residue in fitting data (RMSE)
	b	Uncertainity in SCIAMACHY DCC spectra
	c	Uncertainity in Landsat 8 reflectance calculation

5.2   Discussions and Conclusions

This research work developed two algorithms. The first algorithm identifies Deep

Convective Clouds and determines the absolute gain for the coastal aerosol band and

cirrus band in Landsat 8 using SCIAMACHY spectra as a calibration source. Initially

DCCs scenes were identified from the Landsat 8 archive. Then, in each scene, DCC

pixels were identified using the thermal band (10.8 micron) and reflective band (0.665

micron). To avoid non DCC pixels different spatial and thermal homogeneity thresholds

were used and DCC pixels were identified. Calibration coefficients for coastal aerosol

and cirrus bands were determined. To perform this task, the calibration coefficient from

Landsat 8 reflective bands (band 2, 3, 4, 5) was transferred to the coastal aerosol band

and cirrus band using SCIAMACHY DCC spectra as the calibration transfer medium.

Using this procedure the gain for band 1 was found to be 0.986 ±0.003. This estimate has

high precision thus we can say the gain is off by 1.5% with respect to the reflective bands

(band2, 3, 4, 5). Similarly the gain of the cirrus band was estimated to be 0.98 ±0.0384.

Both the results showed a high level of precision i.e. greater than 96%. In comparison to

the coastal aerosol band the cirrus band showed less precise in estimation. This might

have been caused by varying DCC cloud heights. During this research, the effect of cloud heights wasn't taken in consideration. The MODTRAN simulation was performed to see whether the heights of clouds affect the reflectance in various bands. The simulation showed that that there is a certain amount of variation in reflectance in cirrus band due to change in DCC cloud heights, but this variation is negligible for the coastal aerosol band. The change in reflectance of around 4%can be seen in cirrus band when cloud height changes from 12 km to 19 km. This small variation in reflectance due to variation in cloud heights accounts for the observed variation in the cirrus gain estimate.

The second algorithm determines the relative gain for the cirrus band in Landsat 8 using Deep Convective Clouds. Initially DCC scenes were identified from the Landsat 8 archive. A statistical approach was applied for the cirrus band to estimate relative gain. Relative gains were estimated by averaging the composite detector statistic of identified DCC scenes. The relative gains were applied to L1Rp scenes and their performance was analyzed. The comparison of image quality between DCC gain and default CPF gain was done. The qualitative analysis showed that the image quality was drastically improved after DCC derived gains were applied. Similarly the quantitative analysis showed that streaking was below 0.2 for most of the detectors after DCC gain was applied. The DCC gains outperform the default CPF gains in most of the cases.

5.3   Future Work and Recommendation

The DCC method described here showed that it works well with high precision for reflective bands like the coastal aerosol band and shortwave infrared bands like the cirrus band in Landsat 8. Comparatively the cirrus band shows a higher variation in gain estimate than the coastal aerosol band. More information about different cloud properties

can help to increase the precision level in gain estimate of the cirrus band. This is also verified by the simulation performed with the help of MODTRAN. Further analysis of the error budget and absolute uncertainty involved in this entire process needs to be investigated.

The relative gains were derived using 69 different DCC scenes. The work will be better in a statistical sense, if more DCC scenes are used for derivation. The validation of derived gains was done using a few scenes only in the research. Thus applying this gain to more scenes with a broader range of time is recommended. More investigation needs to be done to understand the observed dependency of gain with the position of FPM in the focal plane array.

BIBLIOGRAPHY

[1] J. R. Schott, *Remote Sensing, The Image Chain Approach*, 2nd edition, United States of America: Oxford University Press, 2007.

[2] R. A. Schowengerdt, *Remote Sensing Models and Methods for Image Processing*, New York, United States of America: Academic Press, 1997.

[3] U.S. Geological Survey. (2014) *Landsat Missions* [Online]. Available: http://landsat.usgs.gov/L8_band_9.php.

[4] Alok Kumar Shrestha, "Relative Gain Characterization and Correction for Pushbroom Sensors Based on Lifetime Image Stastistics and Wavelet Filtering", South Dakota State University, Brookings, SD, Thesis 2010.

[5] Sensing and Processing Centre for Remote Imaging. (2014, July) *Interpretation of Optical Images* [Online]. Available: http://www.crisp.nus.edu.sg/~research/tutorial/opt_int.htm.

[6] Institute for Geoinformatics and Remote Sensing Universitat Osnabruck. (2014, August) *Studienproject 08/09 Evaluation and Integration von Biddaten digitaler Hochleistungskameras* [Online]. Available: http://www.florianhillen.de/studium/projekt/index.php?id=grundlagen&uid=sensoren.

[7] U.S. Geological Survey. (2014) *Landsat - A Global Land-Imaging Mission* [Online]. Available: http://pubs.usgs.gov/fs/2012/3072/fs2012-3072.pdf.

[8] U. S. Geological Survey. (2014, August) *Landsat Missions* [Online]. Available: http://landsat.usgs.gov/landsat8.php.

[9] James R. Irons. (2014, September) *Landsat Science* [Online]. Available: http://landsat.gsfc.nasa.gov/?p=5779.

[10] NASA Official. (2014, August) *Landsat Science* [Online]. Available: http://landsat.gsfc.nasa.gov/?p=3186.

[11] NASA Official. (2014, September) *Landsat Science* [Online]. Available: http://landsat.gsfc.nasa.gov/?p=5775.

[12] U.S. Geological Survey. (2013, February) *LDCM CAL/VAL ALGORITHM DESCRIPTION DOCUMENT* [Online]. Available: http://landsat.usgs.gov/documents/LDCM_CVT_ADD.pdf.

[13] Department of Interior U.S. Geological Survey, "*LDCM Mission Data, Data Format Control Book (DFCB)*", Sioux Falls, USA, South Dakota, LDCM data format control book version 6.0, 2012.

[14] Bo-Cai Gao and Yoram J. Kaufman, "Selection of a 1.3758 um Channel for Remote Sensing of Cirrus Clouds and Stratospheric Aerosols from EOS/MODIS", in *SPIE Proceedings*, Orlando, FL, 1993.

[15] SCIAMACHY-Scanning Imaging Absorption Spectrometer for Atmospheric Chartography. (2014, Spetember) [Online]. Available: www.sciamachy.org.

[16] European Space Agency (ESA), "ENVISAT-1 Products Specifications", ESA, SCIAMACHY Product Specifications 2010.

[17] IUP BREMEN. (2014) *SCIAMACHY* [Online]. Available: http://www.iup.uni-bremen.de/sciamachy/index.html.

[18] Nischal Mishra, "Use of EO-1 Hyperion Data to Perfrom Special Band Adjustment of L7 ETM + and Terra Modis Sensors for Accurate Cross Calibration", South Dakota State University, Brookings, SD, Master Thesis 2011.

[19] K. Throme, B. L. Markham, J. Barker, P.Slater and S. Biggar, "Radiometric Calibration of Landsat", *American Society for Photogrammetry and Remote Sensing*, vol. 63, pp. 853-858, July 1997.

[20] U. S. Geological Survey. (2014, August) *Landsat Missions* [Online]. Available: http://landsat.usgs.gov/science_calibration.php.

[21] Nischal Mishra, Dennis Helder, Amit Angal, Jason Choi and Xiaoxing Xiong, "Absolute Calibration of Optical Satellite Sensors Using Libya 4 Pseudo Invariant Calibration Site", *Remote sensing* , February 2014.

[22] Gyanesh Chander, Brian Markham and Dennis Helder, "Summary of Current Radiometric Calibration Coefficients for Landsat MSS, TM, ETM+, and EO-1 ALI Sensors", *Remote Sensing of Environment*, pp. 893-903, January 2009.

[23] Amit Angal and Dennis Helder, "Advanced Land Imager Relative Gain Characterization and Correction", in *Pecora 16 GLobal Priorities in Land Remote*

sensing, Sioux Falls, South Dakota, 2005.

[24] Earth Resources Observation Systems, "LDCM Level 1 (L1) Data Format Control Book (DFCB)", Sioux Falls, South Dakota, version 6.0, 2012.

[25] B-J. Sohn, Seung-Hee Ham and Ping Yang, "Possibility of the Visible- CHannel Calibration Using Deep Convective Clouds Overshooting the TTL", *American Meterological Society (Journal of Applied Meteorology and Climatology)*, vol. 48, pp. 2271-2283, February 2009.

[26] Steven C. Sherwood, Jung-Hyo Chae, Patrik Minnis and Matthew and McGill, "Underestimation of Deep Convective Cloud Tops by Thermal Imagery", *Geophysical Research Letters*, Feburary 2004.

[27] David R. Doelling, Daniel Morstad, Benjamin R Scarino, Rajendra Bhatt and Arun Gopalan, "The Characterization of Deep Convective Clouds as an Invariant Calibration Target and as a Visible Calibration Technique", *IEEE transactions on Geoscience and remote Sensing*, vol. 51, March 2013.

[28] P. Minnis, "CERES edition-2 Cloud Property re-trievals using TRMM VIRS and Terra and Aqua MODIS data- Part I: Algorithms", *IEEE Transactions on Geoscience and Remote Sensing*, pp. 4374-4400, 2011.

[29] Yongxiang Hu, Bruce A. Wielicki, Ping Yang, Paul W. Stackhouse, Jr, Bin Lin, and David F.Young, "Application of Deep Convective Cloud Albedo Observation to Satellite-Based Study of the Terrestrial Atmosphere: Monitoring the Stability of

Spaceborne Measurements and Assessing Absorption Anomaly", *IEEE Transactions on Geoscience and Remote Sensing*, vol. 42, November 2004.

[30] www.globe.gov. (2014, september) The Globe Program [Online].Available: https://www.globe.gov/globe-gov-home-portlet/images/GLOBE_DetailMap2.png.

[31] Aisheng Wu, Xiaoxiong Xiong, David R. Doelling, Daniel Morstad, Amit Angal and Rajendra Bhatt, "Characterization of Terra and Aqua MODIS VIS, NIR, and SWIR Spectral Band's Calibration Stability", *IEEE Transactions on Geoscience and Remote Sensing*, November 2012.

[32] Dennis Helder, "Comparision of MSS Relative Radiometric Calibration Methods", *SPIE Recent Advances in Sensors, Radiometric Calibration and Processing of Remotely Sensed Data*, vol. 1938, pp. 46-55, 1993.

[33] Dennis Helder, Timothy A. Ruggles, James D. Dewald and Sriharsha Madhavan, "Landsat-5 Thematic Mapper Reflective-Band Radiometric Stability", *IEEE Transactions on Geoscience and Remote Sensing*, vol. 42, December 2004.

[34] Frank Pesta, Suman Bhatta, Dennis Helder and Nischal Mishra, "Radiometric Non-Uniformity Characterization and Correction of Landsat 8 OLI using Earth Imagery-Based Techniques", *Remote Sensing : An Open Acess Journal from MDPI*, 2014.

[35] United States Geolological Survey (USGS). (2014, July) *USGS website* [Online]. Available: http://landsat.usgs.gov/Landsat8_Using_Product.php.

[36] DLR-IMF and IUP-IFE. (2014, September) *SCIAMACHY Operations Support* [Online]. Available: http://atmos.caf.dlr.de/projects/scops/.

[37] B. A. Wielicki, B. R. Barkstrom, E. F. Harrison, R. B. Lee III, G. L. Smith and J. E. Cooper, "Clouds and the Earth's Radiant Energy System (CERES): An Observing System Experiment", *American Metrological Society*, pp. 853-868, 1996.

[38] M. R. Pandya, R. P. Singh, K. N. Chaudhari, K. R. Murali, A.S. Kirankumar, V. K. Dadhwal and J. S. Parihar, "Spectral Characteristics of Sensors Onboard IRS-1D and P6 Satellites: Estimation and Their Infulence on the Surface Reflectance and NDVI", *Journal of Indian Remote Sensing*, vol. 35, 2007.

[39] Julia A. Barsi, Brian L. Markham and Jeffrey A. Pedelty, "The Operational Land Imager: Spectral Response and Spectral Uniformity", *SPIE 8153, Earth Observing Systems*, vol. 8153, September 2011.

[40] B-J. Sohn and Seung-Hee Ham and Ping Yang, "Possibility of the Visible-Channel Calibration Using Deep Convective Clouds Overshooting the TTL", *American Meterological Society*, vol. 48, 2009.

[41] Brain L. Markham, "OLI Radiometric Calibration Summary", USGS, Sioux Falls, Technical Interchange Meeting presentaion slides, 2014.

[42] Disclaimer for SCIAMACHY IPF 7.04 Level 1b Products (SCI_NL_IP). (2011) *ESA Earth Online* [Online]. Available:

https://earth.esa.int/documents/10174/24074/SCI_NL__1P_README.pdf/42e961
d8-dd19-4362-aafb-250bca7f616a?version=1.0.

[43] J. R. schott, "*Remote Sensing, The Image Chain Approach*", vol. 1, no. 1, p. 1,
2010.

[44] U.S. Geological Survey. (2014, september) *USGS Land missions* [Online].
Available: http://landsat.usgs.gov/L8_band_combos.php.

[45] H. Bovensmann, J. P. Burrows, M. Buchwitz, J. Frerick, S. Noel, V. V. Rosanov,
K. V. Chance, and A. P. H. Goede, "SCIAMACHY: Mission Objectives and
Measurement Modes", *Journal of Atmospheric Sciences*, vol. 56, pp. 127-150,
January 1999.

[46] J. Skupin, S. Noel, M. W. Wuttke, M. Gottwald, H. Bovensmann, M. Weber and J.
P. Burrows, "SCIAMACHY Solar Irradiance Observation in the spectral range
from 240 to 2380 nm", *Advances in Space Researches*, vol. 35, pp. 370-375,
2005.

[47] G. Licthtenberg, Q. Kleipool and J. M. Krijger, "SCIAMACHY Level 1 data:
Calibration Concept and Inflight Calibration", *Atmospheric Chemistry and
Physics*, vol. 6, pp. 5347-5367, November 2006.